

## Comparison of in-situ FISH measurements of water vapor in the UTLS with ECMWF (re)analysis data

A. Kunz<sup>1</sup>, N. Spelten<sup>2</sup>, P. Konopka<sup>2</sup>, R. Müller<sup>2</sup>, R. M. Forbes<sup>3</sup>, and H. Wernli<sup>1</sup>

<sup>1</sup>Institute for Atmospheric and Climate Research, ETH Zurich, Zurich, Switzerland

<sup>2</sup>Institut für Energie- und Klimaforschung: Stratosphäre (IEK-7), Forschungszentrum Jülich, Jülich, Germany

<sup>3</sup>European Centre for Medium-Range Weather Forecasts, Reading, UK

*Correspondence to:* A. Kunz  
(anne.kunz@env.ethz.ch)

**Abstract.** An evaluation of water vapor in the upper troposphere and lower stratosphere (UTLS) of the ERA-Interim, the global atmospheric reanalysis produced by the European Centre for Medium-Range Weather Forecasts (ECMWF), is presented. Water vapor measurements are derived from the Fast In-situ Stratospheric Hygrometer (FISH) during a large set of airborne measurement campaigns from 2001 to 2011 in the tropics, midlatitudes and polar regions, covering isentropic layers from 300-400 K (5-18 km).

The comparison shows around 87 % of the reanalysis data are within a factor of two of the FISH water vapor measurements and around 30 % have a near perfect agreement with an over- and underestimation lower than 10 %. Nevertheless, strong over- and underestimations can occur both in the UT and LS, in particular in the extratropical LS and in the tropical UT where severe over- and underestimations up to 10 times can occur.

The analysis data from the evolving ECMWF operational system is also evaluated and the FISH measurements are divided into time periods representing different cycles of the Integrated Forecast System (IFS). The agreement with FISH improves over the time, in particular when comparing water vapor fields for time periods before 2004 and after 2010. It appears that influences of tropical tropospheric and extratropical UTLS processes, e.g., convective and quasi-isentropic exchange processes, are particularly challenging for the simulation of the UTLS water vapor distribution. Both the reanalysis and operational analysis data show the tendency of an overestimation of low water vapor mixing ratio ( $\lesssim 10$  ppmv) in the LS and underestimation of high water vapor mixing ratio ( $\gtrsim 300$  ppmv) in the UT.

## 1 Introduction

Water vapor is **one of the most important greenhouse gases** in the atmosphere and plays a key role in the atmospheric part of the climate system. A change in water vapor, in particular in the upper troposphere and lower stratosphere (UTLS), affects the surface climate and is important for understanding the decadal variability of surface temperatures (Forster and Shine, 1997; Solomon et al., 2010; Riese et al., 2012).

Water vapor is an extremely variable trace gas that is affected by phase transitions from and to liquid and solid hydrometeors. In the UTLS, the formation and sublimation of ice particles in cirrus clouds is particularly relevant. Water vapor is also involved in atmospheric chemistry. In the troposphere it is the prime source of hydroxyl radicals (e.g., Rohrer and Berresheim, 2006) and thus water vapor indirectly controls the lifetime of most gaseous atmospheric pollutants in the atmosphere. In the stratosphere water vapor may be chemically produced through the oxidation of methane (Jones and Pyle, 1984; Röckmann et al., 2004; Rohs et al., 2006). Transport processes in the troposphere play a key role for the distribution of water vapor. In the vicinity of the tropopause and in particular across the subtropical jet stream large gradients of water vapor exist due to the barrier effects of the tropopause (Haynes and Shuckburgh, 2000; Pan et al., 2004; Flentje et al., 2007; Kunz et al., 2011b). In the tropics, the low temperatures at the tropopause lead to strong freeze-drying (Jensen and Pfister, 2004; Fueglistaler et al., 2009; Schiller et al., 2009).

The representation of these UTLS processes is challenging for operational numerical weather prediction (NWP) models and the NWP system from the European Centre for Medium-Range Weather Forecasts (ECMWF) is evaluated here. Besides the operational analysis and forecast cycles, ECMWF has produced different global atmospheric reanalysis products, e.g., ERA-40 from 1957 to 2002 (Upala et al., 2006) and ERA-Interim covering the time period from 1979 to near-real time (Dee et al., 2011).

Validation studies of the ECMWF water vapor fields show that **the operational analysis** and forecasted UTLS water vapor fields might in cases deviate significantly from independent in-situ observations (Flentje et al., 2007; Schäfler et al., 2010). Flentje et al. (2007) evaluated the short-term high resolution ECMWF forecasts by airborne lidar water vapor measurements during the international TROCCINOX campaign. Based on a case study for March 2004 above the tropical and subtropical Atlantic between Brazil and Europe, Flentje et al. (2007) found an overall good reproduction of the observed water vapor distribution. However, locally there were large differences in the vicinity of strong water vapor gradients, a too moist and shallow boundary layer, and an overestimation of convective transport of moisture to the UT. Schäfler et al. (2010) presented a similar case study for operational ECMWF analyses based on measurements during a campaign over western Europe in August 2007. Their comparison of lidar water vapor measurements with ECMWF analyses revealed an overestimate of boundary layer moisture in localized regions over Europe.

A more climatological evaluation of water vapor fields based on the multi-year MOZAIC (Measure-

ments of Ozone and Water Vapour by Airbus In-Service Aircraft) program was presented for the former ERA-40 data set by Oikonomou and O'Neill (2006) and for operational ECMWF analysis fields by Luo et al. (2007). Oikonomou and O'Neill (2006) found for 1991 to 1999 that the ERA-40 mixing ratios of water vapor are considerably larger than observed by MOZAIC, typically by 20 % in the tropical upper troposphere, and by more than 60 % in the lower stratosphere in high latitudes. The moist bias with an overestimation of the extratropical lower stratospheric specific humidity in the ECMWF operational analysis and forecast system has been also intensively studied with CARIBIC (Civil Aircraft for the Regular Investigation of the atmosphere Based on an Instrument Container) in-situ measurements between 2005 and 2012 (Dyroff et al., 2014).

A moist model bias in the extratropical lowermost stratosphere has the potential to impact the temperature distribution including a cold bias near the tropopause (Stenke et al., 2008). It is thus important to improve the moist bias in atmospheric models for the calculation of radiative fluxes, particularly in the stratosphere where absolute humidities are small, but relative errors can be large. The moist model bias analyzed with the MOZAIC measurements may be due to limitations in the ECMWF model, as described by Oikonomou and O'Neill (2006). Anyhow, the exact difference between the model and MOZAIC measurements may also be influenced by the bias in the MOZAIC water vapor observations in the lower stratosphere. The MOZAIC relative humidity sensor has likely a positive bias above the tropopause, compared to high-resolution observations with the Fast In-situ Stratospheric Hygrometer (FISH) (Kunz et al., 2008).

The ERA-Interim water vapor data set has already been used for studies of key atmospheric processes in the UTLS such as the Brewer-Dobson circulation and the double tropopause (Castanheira et al., 2012), or the transport of water vapor from the subtropics toward the extratropics (Ploeger et al., 2013). Anyhow, a detailed evaluation of the ERA-Interim representation of water vapor does not exist and is therefore the main aim of this study. An assessment of the quality of the ERA-Interim water vapor product is particularly relevant for further improving the hydrological cycle in the ECMWF model and for a better understanding and interpretation of diagnostic studies using water vapor fields of this comprehensive data set.

In the following, all available high-resolution in-situ water vapor measurements by the FISH instrument from 2001 to 2011 are used for a comprehensive validation of ERA-Interim water vapor in the UTLS. FISH has successfully participated in a large number of airborne measurement campaigns both in the northern and southern hemisphere during recent years. Data from different measurement campaigns are obtained in polar regions (EUPLEX2003, POLARCAT2008, RECONCILE2010), in midlatitudes (SPURT2001–2003, ENVISAT2002, EUPLEX2003, CIRRUS2003–2006, MACPEX2011), and in the tropics (TROCCINOX2005, SCOUT2005, AMMA2006). Taking the water vapor data of all these measurement campaigns therefore results in a comprehensive data set, referred to here as the FISH-based water vapor climatology, at altitudes from 5 to 18 km, i.e., covering the UTLS. Thus, the FISH-based water vapor climatology is well suited for an evaluation of

the global distribution of ERA-Interim water vapor fields in the UTLS. Since the reanalysis product is based on a single fixed version of data assimilation and forecast model, the ECMWF operational analyses are also considered for the time period of the FISH-based water vapor climatology to study the changes of the UTLS water vapor simulation from changes in the operational forecasting system from 2001 to 2011.

A one-to-one comparison of measured and modeled water vapor fields will lead to 1) a quantification of the agreement between observed and reanalyzed water vapor for specified episodes, and 2) an investigation of the change of the water vapor representation in operational ECMWF analyses. The paper is structured as follows. In section 2 the data base will be described. The FISH measurements, the ERA-Interim and the operational analysis data sets will be introduced and the methodology to compare observations and (re)analyses will be described. The results will be presented in section 3 and finally summarized and discussed in section 4.

## 2 Data Description and analysis methodology

### 2.1 FISH measurements

#### 2.1.1 Measurement technique of FISH

H<sub>2</sub>O mixing ratio is measured in-situ using the FISH instrument (Zöger et al., 1999), which is based on the Lyman  $\alpha$  photo-fragment fluorescence technique. The FISH instrument has been flown on a variety of airborne platforms. It has a forward facing inlet and measures total water, i.e., the sum of the gaseous and the condensed phase. FISH is regularly calibrated in the laboratory against a commercial frostpoint hygrometer. The response time is 1 s, which allows also the detection of small-scale variations of the H<sub>2</sub>O mixing ratio in the vicinity of the tropopause, in clouds and contrails. The instruments accuracy is 7 % and the detection limit is better than 0.3 ppmv. The FISH instrument is therefore particularly suitable for water vapor measurements in the stratosphere where other instruments such as the MOZAIC sensors lose their sensitivity resulting in a moist bias of MOZAIC data compared to FISH measurements in the extratropical LS (Kunz et al., 2008). In all aircraft campaigns the FISH instrument is switched on above a pressure level of roughly 400 hPa. The boundary layer is therefore not captured by the FISH measurements. In the lower troposphere, the measurement cell of FISH becomes optically dense due to large mixing ratios and the FISH fluorescence method is limited on in-situ measurements above a mixing ratio of 500 ppmv. Critical FISH measurements above 500 ppmv ( $\gtrsim 400$  hPa) are therefore excluded from this analysis following Kunz et al. (2008).

### 2.1.2 FISH-based water vapor climatology

For this study we use the data of ten international measurement campaigns with different scientific objectives (see table 1 for an overview). Polar campaigns such as RECONCILE2010 were aimed at a better understanding of polar vortex dynamics and chemical reactions (von Hobe et al., 2013).

130 Other campaigns, such as the eight SPURT campaigns over two years, were intended to observe seasonal differences of various trace gases in the midlatitude tropopause region (Engel et al., 2006), and tropical campaigns such as TROCCINOX2005 investigated the impact of tropical deep convection on the distribution and the sources of trace gases, cloud and aerosol particles in the UTLS (Flentje et al., 2007; Schiller et al., 2009).

135 The resulting FISH-based water vapor climatology extends from 2001 to 2011. It consists of measurements from 148 flights on 136 different days corresponding to more than 600 hours with FISH water vapor data in the UTLS. In this study, only the gas-phase water vapor is used, i.e., water vapor mixing ratios are selected, which are lower than the saturation mixing ratio corresponding to a relative humidity with respect to ice of 100 %. In contrast to the northern hemisphere airborne in-situ  
140 climatology by Tilmes et al. (2010) from 1995 to 2008, only FISH measurements will be considered here, leading to a more homogeneous observational data set based on the same measurement technique. Thus, the FISH-based water vapor climatology proves to be well suited for a model evaluation since the results are not influenced by changing measurement accuracies or height dependent sensitivities of the measurement instrument (Kunz et al., 2008).

145 Figure 1 (panel a) shows the geographical distribution of all measurements included in the FISH-based water vapor climatology. Most of the flights were performed over Europe spanning a region from 30° to 80° N and 10° W to 30° E. In the northern hemisphere, the data set also contains measurements over Greenland obtained in 2008, over the U.S. sampled in 2011 and over Africa in 2006. In the southern hemisphere, the FISH-based water vapor climatology contains measurements over  
150 Brazil and Australia in the year 2005.

The highest frequency of measurements is in the vicinity of the tropopause (Fig. 1, panel b), roughly around 16 to 18 km in the tropics and around 9 to 12 km in the midlatitudes poleward of the subtropical jet stream. In the Arctic, there is also a high frequency of measurements in the deeper stratosphere at around 18 km from campaigns with polar vortex related objectives such as RECON-  
155 CILE2010. There is also a high measurement frequency in the middle troposphere at around 5 km from POLARCAT2008.

### 2.2 ERA-Interim data

The specific humidity from the ERA-Interim reanalysis dataset from the ECMWF (Dee et al., 2011) is evaluated in this paper. The model configuration is based on 60 model hybrid levels with the top of  
160 the atmosphere located at 0.1 hPa and a spectral T255 horizontal resolution. ERA-Interim is based

on IFS release Cy31r2, taken for operational forecasting at ECMWF from 12 December 2006 until 5 June 2007. Dee et al. (2011) gives a comprehensive overview of the ERA–Interim data set, including the data assimilation methodology, the forecast model, and the input observations. Although the observational network changes over time, the reanalysis product is based on a single fixed version of data assimilation and forecast model, in contrast to the changing operational forecasting system. For this study, ERA–Interim data on a  $1^\circ \times 1^\circ$  horizontal grid are used for the 136 days of measurement flights (Table 1 and Fig. 1). The data is then processed as follows:

1. Interpolation of the ERA–Interim specific humidity fields to the positions (latitude, longitude, altitude) of the FISH measurements. For this purpose, 3D backward– and forward trajectories are calculated with the trajectory module of the Chemical Lagrangian Model of the Stratosphere based on a hybrid vertical coordinate system (see McKenna et al. (2002) and Ploeger et al. (2013) for more information on the model and trajectory calculations). These trajectories are initialized at every measurement time and position. After reaching the closest analysis time, i.e., 00, 06, 12, or 18 UTC, the respective latitude and longitude positions of the trajectories are stored. At these positions, vertical interpolation of the ERA–Interim specific humidity field is then performed linearly in potential temperature coordinates. Non-linearity of transport driven by the ERA–Interim wind fields is taken into account. It is thus assumed that during this short advection along the trajectories, i.e., smaller than 3 hours, the specific humidity does not change. The ERA–Interim specific humidity values (in kg/kg) are converted to water vapor volume mixing ratio (in ppmv) by multiplication with the quotient of molar masses of dry air and water, i.e.,  $28.9644/18.015 \times 10^6$ .
2. Vertical interpolation of the ERA–Interim meteorological fields, i.e., zonal wind, meridional wind, temperature and geopotential height, on isentropic surfaces between 280 and 500 K (every 10 K). Afterward, the isentropic static stability and the potential vorticity fields are calculated. The PV values are then transformed into equivalent latitudes. For that purpose, on each isentrope the area enclosed by a PV contour in a hemisphere is transformed to a circle with the same area centered at the pole. The equivalent latitude is the distance in degrees of latitude from the equator to this circle. Afterward, the dynamic tropopause based on the maximum product of PV–gradients and wind speed with equivalent latitude is determined on the different isentropes following Kunz et al. (2011a). The quasi-horizontal distance of the measurement location from the dynamic tropopause is calculated as isentropic difference of the equivalent latitude of the measurement location and the equivalent latitude of the dynamic tropopause along each geographical longitude following Kunz et al. (2011b).
3. ERA–Interim temperature fields are extracted in the entire vertical column of the measurement positions. According to WMO (1957) the location of the thermal tropopause based on the vertical lapse rate is determined and the vertical distance of the measurement location from

the thermal tropopause is calculated in altitude levels.

### 2.3 Operational analysis data

The same procedure as for the ERA–Interim data in section 2.2 is performed for the specific humidity data from the ECMWF operational analysis. From 2001 to 2006 the data is at a resolution of T511L61 (T511 spectral resolution, 61 levels in the vertical). In 2006, the model horizontal and vertical resolution was increased to T799L91 and then to T1279 at the beginning of January 2010. Thus, the horizontal resolution of the operational analysis data are higher than the fixed T255 resolution of ERA–Interim. For comparison reasons, the operational data are also interpolated to a regular  $1^\circ \times 1^\circ$  horizontal grid. From 2001 to 2011 there have been multiple model changes from IFS Cycle 23r4 in June 2001 (also used for the former reanalysis product ERA–40), to Cycle 37r3 in November 2011 (see section 2.4 for model changes relevant to the humidity during this period). The comparison of the operational analysis water vapor with the FISH observations will therefore be performed on a daily basis (see Section 4). For the evaluation of the temporal change in water vapor representation in operational ECMWF analyses two time intervals almost representing two years each are investigated: time interval 1 (Cy28r1–Cy30r1) from March 2004 to August 2006 and time interval 2 (Cy36r1–Cy36r4) from January 2010 to April 2011. These intervals are chosen since they are well represented by the FISH measurements and a comparison will further show the change in water vapor representation before and after the IFS release Cy31r2 that is used for ERA–Interim.

### 2.4 Changes to the IFS over time

During the period 2001 to 2011 considered here, there have been a number of changes to the IFS that potentially affect the humidity field and representation of the hydrological cycle. The most significant changes are briefly described here although not all humidity impacts have been documented.

In Cycle 26r3 (2003) a new humidity analysis scheme was implemented (Hólm, 2002) with a nonlinear transformation of the humidity control variable to render the humidity background errors more nearly Gaussian. The modifications to the formulation of the humidity analysis and its impact on the assimilation of humidity-sensitive observations are described by Andersson et al. (2005).

In Cycle 31r1 (2006) just before the ERA–Interim cycle, a revised cloud scheme was introduced including a new parameterization of supersaturation with respect to ice for temperatures lower than 250 K in the cloud-free part of the grid box (Tompkins et al., 2007). The introduction of ice supersaturation delayed the formation of ice clouds and the upper tropospheric humidity increased in the forecast model (Tompkins et al., 2007). However, the degree of ice supersaturation was limited in the four-dimensional variational assimilation (4DVAR) scheme leading to a spin up of humidity from the analysis into the forecast (Lamquin et al., 2009).

Cycle 32r3 (2007) included revisions to the free tropospheric diffusion and to the convection scheme, in particular the introduction of a variable convective adjustment time-scale and a convective en-

trainment rate proportional to the environmental relative humidity (Bechtold et al., 2008). This cycle resulted in a significantly higher and more realistic level of model activity in terms of the amplitude of tropical and extratropical mesoscale, synoptic and planetary perturbations with impacts on the UTLS temperature and humidity. This cycle also included a new bias-correction scheme for radiosonde temperature and humidity data as a function of solar elevation and radiosonde type.

In Cycle 35r3 (2009), ice supersaturation was allowed fully in the 4DVAR analysis leading to an increase in upper tropospheric humidity in the analysis. Finally, Cycle 36r4 (2010) introduced a new cloud scheme with separate prognostic variables for ice cloud, liquid cloud, rain and snow (Forbes et al., 2011) and resulted in some drying of the upper tropospheric humidity into the forecast. Note that in the IFS analysis system, no humidity increments are allowed in the stratosphere which means the distribution of humidity is determined primarily in the forecast model by tropospheric exchange, by upper-level moistening due to methane oxidation and by advection.

## 2.5 Ratio of water vapor between (re)analysis fields and FISH

The ratio between the ECMWF water vapor, e.g., the reanalysis water vapor  $H_2O_{ERA}$ , and the measured FISH water vapor,  $H_2O_{FISH}$ , is calculated as followed:

$$\Delta H_2O_{ERA} = H_2O_{ERA} / H_2O_{FISH} . \quad (1)$$

A value of  $\Delta H_2O_{ERA} = 1$  indicates a perfect agreement between ERA-Interim and FISH water vapor mixing ratio. The ratio  $\Delta H_2O_{ERA}$  is an asymmetric quantity, i.e., underestimations are related to  $\Delta H_2O \in (0, 1]$  and overestimations to  $\Delta H_2O \in [1, \infty)$ . This asymmetry has influences on statistical quantities like mean values. Therefore, the detailed analysis of modeled and observed water vapor is based on the logarithm of  $\Delta H_2O_{ERA}$  with base 2, i.e.,

$$\Delta H_2O_{ERA}^{\log 2} = \log_2(\Delta H_2O_{ERA}) . \quad (2)$$

A perfect agreement between the model and observations is now indicated by  $\Delta H_2O_{ERA}^{\log 2} = 0$ , underestimations are given by  $\Delta H_2O_{ERA}^{\log 2} \in (-\infty, 0]$  and overestimations by  $\Delta H_2O_{ERA}^{\log 2} \in [0, \infty)$ . Equation 2 is also applied to the operational analysis water vapor  $H_2O_{ANA}$  and the correspondent ratio is referred to as  $\Delta H_2O_{ANA}^{\log 2}$ . Figure 2 presents the relationship between Equ. 1 and Equ. 2 based on the most relevant values for this paper. In particular,  $\Delta H_2O^{\log 2}$  values of 1, 1.6, 2, and 3.32 correspond to a model water vapor mixing ratio that is two, three, four, and ten times larger than the observed water vapor mixing ratio.

The influence of the FISH measurement uncertainty on the ratio  $\Delta H_2O^{\log 2}$  is lower than 22 %. According to section 2.1.1 we assume an instrument accuracy of 7 % and a detection limit of 0.3 ppmv for the two water vapor mixing ratios  $H_2O_{FISH} = 4$  ppmv and  $H_2O_{FISH} = 100$  ppmv. An overestimation of these water vapor mixing ratios of  $\Delta H_2O^{\log 2} = 1$  is therefore connected with an uncertainty range between 0.80 and 1.22 for  $H_2O_{FISH} = 4 \pm 0.58$  ppmv and with an uncertainty range between 0.89 and 1.11 for  $H_2O_{FISH} = 100 \pm 7.3$  ppmv. The ranges where ECMWF data



are undiscriminable from the measured data, i.e.,  $\Delta H_2O^{\log 2} = 0$ , are between -0.20 and 0.23 for  $H_2O_{FISH} = 4 \pm 0.24$  ppmv and -0.10 and 0.11 for  $H_2O_{FISH} = 100 \pm 8$  ppmv.

## 2.6 An example flight

Figures 3 and 4 present the methodology of the ratio of water vapor between (re)analysis fields and FISH for an example flight path during the MACPEX2011 campaign. This flight took place on 1 April 2011 over the U.S. between  $15 - 40^\circ$  N. There are two special characteristics of this flight (see Fig. 3 panel a): 1) A two-times crossing of the subtropical jet stream on the southward direction of the flight (18:00–19:00 UTC) and on the backward flight in northward direction (20:30–21:30 UTC). 2) The flight also probed air masses in the close vicinity of the thermal tropopause on altitudes between 13 and 18 km. Thus, measurements are collected both in the troposphere and stratosphere with different characteristics of the static stability,  $H_2O_{FISH}$  and the interpolated  $H_2O_{ERA}$  and  $H_2O_{ANA}$  along the flight track (Fig. 3, panel b).

For a quantification of these deviations in water vapor mixing ratio between the model and observations the ratio  $\Delta H_2O^{\log 2}$  is shown both for  $H_2O_{ANA}$  and  $H_2O_{ERA}$  in Fig. 4 (panel a). For this example flight both  $\Delta H_2O_{ANA}^{\log 2}$  and  $\Delta H_2O_{ERA}^{\log 2}$  vary between -1 and 1. Thus, there are regions with ECMWF underestimations where  $H_2O_{FISH}$  is twice as large as  $H_2O_{ERA}$ , but also overestimations with  $H_2O_{ERA}$  twice as large as  $H_2O_{FISH}$ . Around 70 % of the values are close to  $\Delta H_2O^{\log 2} = 0$  and thus represent a nearly perfect relationship. The ascent and descent parts of the flight in the troposphere (before 18:00 UTC and after 21:45 UTC), and the parts in the vicinity of the equatorward side of the subtropical jet stream (19:00–19:30 UTC and 20:15–20:45 UTC) clearly show an enhanced  $\Delta H_2O^{\log 2}$  with a ratio up to 2. Here, the ECMWF water vapor may be twice as large as the observations. A fairly good agreement with  $\Delta H_2O \approx 0$  is observed in regions where the airplane samples stratospheric air masses, e.g., from 18:00–18:30 UTC and from 21:00–21:30 UTC. Largest deviations appear in air masses of the middle tropical troposphere at around 12 km, e.g., at 20:00 UTC, when the ECMWF underestimates the observed water vapor content.

The mean water vapor mixing ratio per  $\Delta H_2O^{\log 2}$  bin shows that  $H_2O_{ANA}$  and  $H_2O_{ERA}$  overestimate  $H_2O_{FISH}$  at lower mixing ratios than 10 ppmv and underestimate  $H_2O_{FISH}$  for higher mixing ratios than 30 ppmv (Fig. 4, panels b and c). When comparing  $H_2O_{ERA}$  and  $H_2O_{ANA}$  in more detail (Fig. 4, panel a) the measurements are better represented by  $H_2O_{ANA}$  than by  $H_2O_{ERA}$  in the middle troposphere and close to the jet stream roughly between 19:15–20:45 UTC. This may well be explained by an improvement of the ECMWF data assimilation system over four years.  $H_2O_{ERA}$  is based on the IFS release Cy31r2 in 2007 and  $H_2O_{ANA}$  on Cy36r1 in 2011. However, there are regions in the stratosphere with water vapor mixing ratios lower than 5 ppmv where  $H_2O_{ERA}$  slightly better represents  $H_2O_{FISH}$  than  $H_2O_{ANA}$ .

### 3 Water vapor evaluation: ERA–Interim vs. FISH

Taking all measurements together, around 30 % of the data are very well represented by the model with  $\Delta H_2O_{ERA}^{\log^2}$  between -0.15 and 0.15, i.e., there is a deviation of lower than 10 %. The majority of the data, i.e., 57 %, are within the  $\Delta H_2O_{ERA}^{\log^2}$  bins -1 to -0.15 and 0.15 to 1, and 13 % are connected with a severe under- ( $\Delta H_2O_{ERA}^{\log^2} < -1$ ) or overestimation ( $\Delta H_2O_{ERA}^{\log^2} > 1$ ). Over- and underestimations are found both in the stratosphere and troposphere, whereas the troposphere is characterized by larger deviations than the stratosphere. This is discussed in more detail in the following sections.

#### 3.1 Campaign–based analysis

Since the measurement campaigns represent different geographical and altitude regions (see Fig. 1) the comparison between ERA–Interim and FISH water vapor is first performed for each campaign separately.

Figure 5 (left panels, respectively) shows the frequency distribution of  $\Delta H_2O_{ERA}^{\log^2}$  for each campaign. The range of  $\Delta H_2O_{ERA}^{\log^2}$  is between -3.3 and 3.3 and its bin size is variable to represent reasonable scales as shown Fig. 2. In general,  $\Delta H_2O_{ERA}^{\log^2}$  values between -2.8 and 2.3 are found, i.e., the model occasionally underestimates the observations up to a factor 7 and overestimates them up to a factor 5. Dependent on the campaign, around 10-20 % of the data are within a  $\Delta H_2O_{ERA}^{\log^2}$  range between -0.15 and 0.15 indicating an almost perfect agreement between the reanalyses and observations. The majority of the data, i.e., around 40-80 %, are within the  $\Delta H_2O_{ERA}^{\log^2}$  ranges of -1.0 to -0.15 and 0.15 to 1.0 indicating a fairly good agreement. **Both the mean and median values of  $\Delta H_2O_{ERA}^{\log^2}$  are close to each other at  $\Delta H_2O_{ERA} \approx 0$  for all campaigns.** The range of the mean of  $\Delta H_2O_{ERA}^{\log^2}$  is **varying** from -0.19 (SPURT2001-2003) to 0.43 (POLARCAT2008). The standard deviation of  $\Delta H_2O_{ERA}^{\log^2}$  ranges from 0.23 (RECONCILE2010) to 0.99 (SPURT2001-2003). In particular the SPURT campaigns, which contain data from different seasons and atmospheric situations have a larger variance around the mean than campaigns like RECONCILE2010, which include data from one single season and a polar vortex oriented flight strategy (von Hobe et al., 2013).

Figure 5 (right panels, respectively) shows the mean  $H_2O_{ERA}$  and  $H_2O_{FISH}$  per  $\Delta H_2O_{ERA}^{\log^2}$  bin. The mean mixing ratios corresponding to a near perfect agreement with  $\Delta H_2O_{ERA}^{\log^2}$  between -0.15 and 0.15 range from 7 ppmv (e.g., SCOUT2005, ENVISAT2002-2003, EUPLEX2003, and RECONCILE2010) to 300 ppmv (e.g., POLARCAT2008). This indicates that ERA–Interim shows accurate water vapor values for both very dry and much moister conditions. There are campaigns, e.g., TROCCINOX2005, where ERA–Interim significantly underestimates the measurements at water vapor mixing ratios larger than 50 ppmv, and overestimates the measurements for mixing ratios lower than 50 ppmv. A similar relation for different water vapor values is shown for AMMA2006 also in the tropics and RECONCILE2010 in polar regions. Other campaigns, e.g., ENVISAT2002-2003 and EUPLEX2003, do not show this relationship and ERA–Interim over- and underestimates

measurements larger than 50 ppmv.

In summary, a fairly good agreement of mixing ratios with  $\Delta H_2O_{ERA}^{\log 2} \approx 0$  occurs both at low mixing ratios, e.g., at  $H_2O \approx 10$  ppmv for the TROCCINOX2005 campaign, but also at high mixing ratios, e.g.,  $H_2O \approx 300$  ppmv for the POLARCAT2008 campaign. Based on this evaluation of individual measurement campaigns there is generally an increasing underestimation towards higher FISH mixing ratios and an increasing underestimation towards lower mixing ratios. To gain insight into the regions of the UTLS where exactly over- and underestimations occur, i.e., in the troposphere or in the stratosphere, the data of all campaigns is now analyzed relative to the positions of the tropopause and upper-tropospheric jet streams.

### 3.2 Tropopause-based analysis in three atmospheric domains

Following Kunz et al. (2013) the measurement locations are divided into three atmospheric domains with respect to the height of the thermal tropopause ( $TP_H$ ). In the climatological mean, the tropics are characterized by a thermal tropopause height above 14 km, whereas in the extratropics tropopause heights are usually lower than 12 km. Consequently, the tropical and the extratropical domains are separated by the subtropical jet stream characterized by an intermediate tropopause height between 12 and 14 km. The FISH-based climatology is therefore analyzed with respect to the three atmospheric domains:

- Tropical measurements (TROP):  $TP_H > 14$  km
- Subtropical measurements (SUBTROP):  $12 \text{ km} \leq TP_H \leq 14 \text{ km}$
- Extratropical measurements (EXTROP):  $TP_H < 12$  km

The separation of the FISH-based water vapor climatology according to these three domains attributes 26 % of data to the tropical, 17 % to the subtropical, and 57 % to the extratropical domain. The proposed selection allows a detailed look at  $\Delta H_2O_{ERA}^{\log 2}$  for tropical and extratropical measurement locations without mixing dynamical processes on the equatorward and poleward side of the subtropical jet stream (see Fig. 1, panel b). In addition, subtropical measurements in the vicinity of the subtropical jet stream are separately considered. For example, the measurements in-between the double tropopauses in the vicinity of the subtropical jet streams during the example MACPEX flight (see Fig. 3, panel b, 18:00 and 21:30 UTC) are characterized by a thermal tropopause of around 13 km and are consequently assigned to the subtropical domain.

Figure 6 (panels a, d, and g) shows  $\Delta H_2O_{ERA}^{\log 2}$  and the counts of measurements for the three atmospheric domains with respect to the distance from the thermal tropopause. The counts are calculated for 1 km thick layers and the  $\Delta H_2O_{ERA}^{\log 2}$  bins are organized as for Fig. 5. Measurements have been made between  $-10$  to  $5$  km around the tropopause in the tropical domain, between  $-6$  to  $8$  km in the subtropical domain, and between  $-6$  to  $10$  km in the extratropical domain. Clear measurement frequency maxima are found in the vicinity of the tropopause in the tropical and extratropical domain.

There is a second frequency maximum found between 6 to 9 km above the tropopause in the extra-tropical domain that is probably related to polar campaigns (see Fig. 1). The subtropical domain is characterized by a relatively uniform vertical distribution of measurements with no pronounced maximum near the tropopause. These distributions show the representativeness of individual tropopause  
 375 and  $\Delta H_2O_{ERA}^{\log 2}$  bins and should be kept in mind when analyzing the key results in the following.

In all three atmospheric domains, over- and underestimations of the measurements are found in the entire UTLS. The measurement frequency peaks near the tropopause are associated with values of  $\Delta H_2O_{ERA}^{\log 2}$  that are ranging between -1.0 and 1.0. The LS of the tropical domain is characterized by those values of  $\Delta H_2O_{ERA}^{\log 2}$  on isentropes above 370 K (Fig. 6, panels a and b). Toward the extratrop-  
 380 ics, severe over- and underestimations are found in the LS. The subtropical domain is characterized by a  $\Delta H_2O_{ERA}^{\log 2}$  roughly between -2.0 and 2.0 on isentropes above 350 K in the LS (Fig. 6, panels d and e) and the extratropical domain shows even stronger over- and underestimations in the LS and  $\Delta H_2O_{ERA}^{\log 2}$  extends between -3.3 to 2.0 on isentropes above 330 K (Fig. 6, panels g and h). Thus, the moist bias of the ECMWF model in the LS that is discussed in the literature is stronger in the  
 385 extratropics than in the tropics. Anyhow, there is also a dry bias of the model in the LS that is of comparable size as the moist bias.

In the tropical domain, the range of  $\Delta H_2O_{ERA}^{\log 2}$  is lower in the LS than in the UT (Fig. 6, panels a-c). The UT of the tropical domain is characterized by  $\Delta H_2O_{ERA}^{\log 2}$  values ranging between -3.3 and 2.8, i.e., underestimations with  $H_2O_{ERA}$  ten times lower than  $H_2O_{FISH}$  and overestimations  
 390 with  $H_2O_{ERA}$  up to seven times larger than  $H_2O_{FISH}$  can be found in the tropical UT. The UT of the subtropical and extratropical domains are not characterized by such strong model deviations as in the tropical domain. Here,  $\Delta H_2O_{ERA}^{\log 2}$  is comparable between the UT and LS (Fig. 6, panels d-i). Finally, strongest over- and underestimations with ERA-Interim more than twice as large or more than half as large as the FISH measurements are found in particular in the tropical UT and extrat-  
 395 ropical LS. Strong underestimations, i.e.,  $\Delta H_2O_{ERA} < -1.0$ , in the UT are connected with a FISH water vapor mixing ratios  $> 300$  ppmv (Fig. 6, panels c, f, and i). Very low FISH water vapor mixing ratios  $< 10$  ppmv in the LS up to 3 km above the tropopause are overestimated with a  $\Delta H_2O_{ERA}^{\log 2}$  up to 1.0 in the tropical domain and up to 2.0 in the subtropical and extratropical domains.

Thus, over- and underestimations are found both in the UT and LS with a rather comparable strength  
 400 of a dry and moist bias. In the tropics the spread of  $\Delta H_2O_{ERA}^{\log 2}$  increases with increasing water vapor mixing ratio from the LS toward the UT (Fig. 6, panel c). This is also reflected by the correlation between  $H_2O_{ERA}$  and  $H_2O_{FISH}$  (Fig. 7, panel a). Thus, the correlation between  $H_2O_{ERA}$  and  $H_2O_{FISH}$  gets weaker toward higher water vapor mixing ratios in the tropical domain. This relationship is weaker in the subtropical and extratropical domains (Fig. 7, panels b and c) where  
 405  $\Delta H_2O_{ERA}^{\log 2}$  is of rather comparable size in the UT and LS.

### 3.3 Equivalent latitude-based analysis on isentropes

The potential temperature and equivalent latitude coordinates provide an isentropic view on the relation between  $H_2O_{ERA}$  and  $H_2O_{FISH}$  (Fig. 8). Here, the isentropic concept of equivalent latitude is used to reduce the effects of reversible transport processes such as tropospheric and stratospheric intrusions connected to the dynamic tropopause in the UTLS (Olsen et al., 2010; Pan et al., 2012). The location of the dynamic tropopause based on the maximum isentropic PV-gradients is determined according to Kunz et al. (2011a) (see also Section 2.2). This PV-gradient based tropopause well represents the dynamical and chemical discontinuity between the UT and LS (Kunz et al., 2011a,b). Thus, it is **located** in the vicinity of the core of the subtropical jet stream on isentropes between 320 to 380 K (Fig. 8, panel a). Figure 9 presents the quasi-horizontal distance of the FISH measurements in equivalent latitude from the PV gradient-based tropopause on isentropes between 300 and 380 K. Negative values represent measurements on the equatorward side of the jet stream in the troposphere and positive values on the poleward side of the jet stream in the stratosphere (see also Kunz et al. (2011b); Pan et al. (2012)).

The highest frequency of FISH measurements can be found near the location of the jet stream and the dynamic tropopause in particular on isentropes between 310 and 370 K (Fig. 8, panel a). This area of high sampling frequency of  $H_2O_{FISH}$  extends on equivalent latitudes up to  $\pm 20^\circ$  around the dynamic tropopause and is related to a  $\Delta H_2O_{ERA}^{log2}$  between -1.0 and 1.0 (Fig. 8 panel b and Fig. 9 panel a).

In line with previous results, over- and underestimations in the UTLS are found on middle world isentropes both poleward and equatorward of the subtropical jet stream. In general, the mean  $\Delta H_2O_{ERA}^{log2}$  per potential temperature and equivalent latitude bin shows overestimations with  $H_2O_{ERA}$  three times larger than  $H_2O_{FISH}$  and underestimations up to ten times corresponding to a mean  $\Delta H_2O_{ERA}^{log2}$  varying between -3.3 and 1.6 (Fig. 8, panel b). Severe underestimations with a mean  $\Delta H_2O_{ERA}^{log2}$  between -3.3 and -1.0 can be found in the LS on isentropes above 360 K at equivalent latitudes poleward of  $60^\circ$  N. The strongest overestimations with a mean mean  $\Delta H_2O_{ERA}^{log2}$  up to 1.6 are also found in the LS poleward of the subtropical jet stream on the 340 K isentrope. Both areas are characterized by a mean  $H_2O_{FISH}$  between 10 and 50 ppmv (Fig. 8, panel c).

On the isentropes between 320 and 340 K, there are two areas in the UT around  $20^\circ$  southward of the dynamic tropopause that are connected with a mean  $H_2O_{FISH}$  higher than 300 ppmv (Fig. 9, panel c). One of these areas of high  $H_2O_{FISH}$  in the UT is overestimated and the other one is underestimated by the model (Fig. 9, panel b). Hereby, the underestimation with  $\Delta H_2O_{ERA}^{log2}$  up to -3.3 is stronger than the overestimation up to 2.0. In contrast, a mean  $H_2O_{FISH}$  of lower than 10 ppmv in the LS up to  $50^\circ$  northward of the dynamic tropopause are largely overestimated by ERA-Interim with  $\Delta H_2O_{ERA}^{log2}$  up to 2.0 (Fig. 9, panel c).

#### 4 Water vapor evaluation: operational analyses vs. FISH

Using the FISH-based water vapor climatology the temporal development of the quality of the ECMWF operational analyses in terms of water vapor in the UTLS is analyzed for the three atmospheric domains. This is done separately for measurements in the stratosphere above the thermal

tropopause (Fig. 10) and in the troposphere below the thermal tropopause (Fig. 11). Since differ-

ent IFS cycles became operational during the eleven years from 2001 to 2011, the daily mean ratio between the operational analysis and FISH water vapor,  $\Delta H_2O_{ANA}^{\log 2}$ , is presented. In addition, the range between the maximum and minimum  $\Delta H_2O_{ANA}^{\log 2}$  is presented for each single measurement day. For comparison, the daily mean  $\Delta H_2O_{ERA}^{\log 2}$  is also discussed, which represents the IFS cycle

31r2, taken for operational forecasting from 12 December 2006 until 5 June 2007.

Over the entire period between 2001 and 2011 the daily mean  $\Delta H_2O_{ANA}^{\log 2}$  varies between -1.0 and 1.0 within the stratosphere of the tropical domain (Fig. 10, panel a). The daily mean  $\Delta H_2O_{ANA}^{\log 2}$  varies stronger in the LS of the subtropical and extratropical domains (Fig. 10, panels d and g). In particular, from 2001 to the end of 2003 the daily mean  $\Delta H_2O_{ANA}^{\log 2}$  varies between -2.0 and 1.0 in

the extratropical domain, i.e., the model more strongly underestimates than overestimates most of the measurements. During this time period, observations are mainly from the SPURT campaign in different seasons, which may likely have an influence on the variability of the daily mean  $\Delta H_2O_{ANA}^{\log 2}$  from 2001 to 2003. Comparing the daily mean  $\Delta H_2O_{ANA}^{\log 2}$  between the time periods before 2004 and after 2009 shows that  $\Delta H_2O_{ANA}^{\log 2}$  yields a value close to the perfect agreement  $\Delta H_2O \approx 0$  more often in the later period, in particular in the tropical LS (Fig. 10, panel a).

Figure 10 (middle and right column) shows the correlation of  $H_2O_{FISH}$  with  $H_2O_{ANA}$  and with  $H_2O_{ERA}$  for two selected time periods with IFS cycles 28r1-31r1 (09 March 2004 to 12 September 2006) and IFS cycles 36r1-37r2 (26 January 2010 to 18 May 2011). There is the tendency that strong overestimations with  $\Delta H_2O_{ANA}^{\log 2} > 1.00$  are related to  $H_2O_{FISH}$  of lower than 5 ppmv. This is observed for IFS cycles 28r1-31r1 and 36r1-37r2, e.g., in the subtropical domain (e.g., Fig. 10, middle row). Thus, the tendency of the model to overestimate low mixing ratios remain for both IFS cycles.

In contrast, underestimations with a  $\Delta H_2O_{ANA}^{\log 2} < -1.00$  are observed for measurements higher than 20 ppmv. These strong deviations from the measurements are found in the LS of the subtropical and extratropical domains of IFS cycles 36r1-37r2 (Fig. 10, panels f and i). The LS of the subtropical domain shows that strong overestimations are reduced with a better  $H_2O_{ANA}$  than  $H_2O_{ERA}$  for measurements higher than 20 ppmv of IFS cycles 36r1-37r2 (Fig. 10, panel f). These areas of improvement in the operational analysis data can be traced back solely on measurements performed during the MACPEX campaign in 2011, e.g., the MACPEX flight on 11 April 2011 (Fig. 12, panels a and c). A detailed study of this flight shows in the subtropical LS with  $H_2O_{FISH} > 20$  ppmv a clear improvement with  $H_2O_{ANA}$  better representing  $H_2O_{FISH}$  than  $H_2O_{ERA}$  between 18:25-18:35 UTC (Fig. 12, panel b). The measurements during that time period are influenced by the presence of a second thermal tropopause in the LS (Fig. 12, panel a). In addition, these measurements are

performed in the vicinity of the thermal tropopause where large gradients of  $\text{H}_2\text{O}$  appear. This is a further case study besides the example shown in Figs. 3 and 4, which may well show the improvement of the later model cycle compared to the model cycle used for ERA–Interim.

In the troposphere, there is also strong variability of the daily mean  $\Delta\text{H}_2\text{O}_{\text{ANA}}^{\log 2}$  from 2001 to 2011 both in the tropical and the extratropical domain (Fig. 11, top and bottom row). In the first years after 2007 the range of  $\Delta\text{H}_2\text{O}_{\text{ANA}}^{\log 2}$  in the extratropical troposphere increases, which may be due to the increased amplitude of tropical and extratropical mesoscale, synoptic and planetary perturbations after the model changes to convection and diffusion parameterization. The increase of  $\Delta\text{H}_2\text{O}_{\text{ANA}}^{\log 2}$  after 2007 is weaker in the extratropical stratosphere than in the extratropical troposphere (Figs. 10 and 11, bottom row). This may be due to the fact that humidity data is not assimilated above the tropopause. Anyhow, other changes of data assimilation and model resolution may contribute to the observed increase of  $\Delta\text{H}_2\text{O}_{\text{ANA}}^{\log 2}$  in the extratropical troposphere after 2007.

When comparing  $\Delta\text{H}_2\text{O}_{\text{ANA}}^{\log 2}$  between the stratosphere and the troposphere for single years, e.g., 2006, there is the tendency that the tropical troposphere is characterized by a larger variance of  $\Delta\text{H}_2\text{O}_{\text{ANA}}^{\log 2}$  than the tropical stratosphere (Figs. 10 and 11, top rows). In contrast, the extratropical troposphere is characterized by a lower variance of  $\Delta\text{H}_2\text{O}_{\text{ANA}}^{\log 2}$  than the extratropical stratosphere, in particular for the period before 2004 (Figs. 10 and 11, bottom rows). This may well show the difficulty to accurately simulate the influence of tropical tropospheric processes as well as extratropical stratospheric processes on the water vapor distribution. Similar to the stratosphere, the correlation of  $\text{H}_2\text{O}_{\text{FISH}}$  and  $\text{H}_2\text{O}_{\text{ANA}}$  in the troposphere shows the tendency of the model to overestimate low and underestimate high mixing ratios (Fig. 11, middle and right columns). The tendencies in over- and underestimations are also observed in the UT of the case study in Fig. 12 (panel b) during the between 18:00–18:15 UTC and 18:45–19:00 UTC. These time periods indicate no clear improvement of the model cycle since  $\text{H}_2\text{O}_{\text{FISH}}$  is not better represented by  $\text{H}_2\text{O}_{\text{ANA}}$  than by  $\text{H}_2\text{O}_{\text{ERA}}$  for large parts of this flight. Thus, there is no clear improvement of the operational analyses compared to ERA–Interim, indicating that problems remain irrespective of the data assimilation cycle and model resolution.

## 5 Summary and Discussion

The latest reanalysis product, the ERA–Interim data set, and the operational analysis product by the ECMWF are evaluated using the global FISH–based water vapor climatology. This climatology represents a valuable data set of high-quality airborne water vapor measurements performed during ten aircraft campaigns from 2001 to 2011 (see Table 1). The advantage of the FISH–based water vapor climatology is that water vapor is measured with a high accuracy throughout the entire UTLS, a region where satellite data have difficulties to accurately measure trace gas distributions. The FISH–based water vapor climatology allows a detailed evaluation of simulated water vapor fields



separately for tropical and extratropical regions.

The UTLS distribution of ECMWF (re)analysis water vapor fields is evaluated using novel analysis  
515 methods. Tropical, subtropical, and extratropical domains are identified according to their characteristic thermal tropopause heights, i.e., larger than 14 km and lower than 12 km. The ratio between modeled and observed water vapor mixing ratio is presented in different coordinate systems, i.e., in relative vertical distances with respect to the thermal tropopause and in relative equivalent distances on isentropes with respect to the dynamic tropopause. These different considerations are well suited  
520 for the interpretation of the possible influence through diabatic or adiabatic dynamical processes, i.e., cross-isentropic and isentropic transport, respectively.

The two main aims of this study are the quantification of the agreement between observed and re-analyzed (ERA–Interim) water vapor fields and the investigation of the change of the water vapor representation in ECMWF operational analyses for time periods with different IFS cycles. The main  
525 results from this work are:

- There is generally a good agreement between ERA–Interim and FISH water vapor mixing ratio, i.e.,  $H_2O_{\text{FISH}}$  and  $H_2O_{\text{ERA}}$ , in most parts of the UTLS. The ratio  $\Delta H_2O_{\text{ERA}}^{\log 2}$  is between -1.0 and 1.0 for around 87 % of all observations, i.e.,  $H_2O_{\text{ERA}}$  may be half or twice as large as  $H_2O_{\text{FISH}}$ . About 30 % of these measurements are nearly perfectly represented by the model  
530 with  $\Delta H_2O_{\text{ERA}}^{\log 2}$  between -0.15 and 0.15, i.e., positive and negative deviations are lower than 10 %. However, ERA–Interim significantly over- and underestimates the FISH measurements for 13 % of the data with  $\Delta H_2O_{\text{ERA}}^{\log 2}$  values of -3.3 or 3.3, i.e., the model may be ten times lower or higher than the observations.
- The tropical LS is well represented by the model, i.e.,  $\Delta H_2O_{\text{ERA}}^{\log 2}$  is between -1.0 and 1.0 in the  
535 region between the thermal tropopause up to 5 km above. This result is in particular reflected on isentropes above 370 K on the equatorward side of the dynamic tropopause. In contrast, the tropical UT is characterized by severe over- and underestimations. In the region between 9 km below the thermal tropopause up to the thermal tropopause  $\Delta H_2O_{\text{ERA}}^{\log 2}$  is observed between -3.3 and 3.3. Here, this result is verified for a large isentropic range between 310 up to 370 K on  
540 the equatorward side of the subtropical jet stream. Convective processes in the entire tropical troposphere may be a reasonable dynamical process responsible for those severe deviations between  $H_2O_{\text{ERA}}$  and  $H_2O_{\text{FISH}}$  over a large range of isentropes.
- In the extratropical LS on altitudes higher than 4 km above the thermal tropopause the deviations between  $H_2O_{\text{ERA}}$  and  $H_2O_{\text{FISH}}$  are similar to the tropical LS, i.e.,  $\Delta H_2O_{\text{ERA}}^{\log 2}$  varies  
545 between -1.0 and 1.0. Anyhow, in the entire region  $\pm 4$  km around the thermal tropopause the values of  $\Delta H_2O_{\text{ERA}}^{\log 2}$  vary between -3.3 and 2.0, i.e.,  $H_2O_{\text{ERA}}$  may be ten times lower or four times larger than  $H_2O_{\text{FISH}}$  near the extratropical tropopause. Dynamical processes playing a role in the vicinity of the thermal tropopause as isentropic exchange processes between the



UT and LS may favor these large model deviations in the extratropical UTLS.

- 550 – There is the tendency of an overestimation of low water vapor mixing ratios and an underestimation of high water vapor mixing ratios. In particular,  $H_2O_{FISH}$  of higher than 300 ppmv in the UT on the equatorward side of the subtropical jet stream within the tropics, subtropics and extratropics are connected with a severe underestimation related to a  $\Delta H_2O_{ERA}^{\log 2}$  up to -3.3. In contrast, most of the  $H_2O_{FISH}$  that is lower than 10 ppmv in the LS is overestimated.
- 555 Here, the overestimation is lower in the tropics ( $\Delta H_2O_{ERA}^{\log 2}$  up to 1.0) than in the subtropics or extratropics ( $\Delta H_2O_{ERA}^{\log 2}$  up to 3.3). Thus, the moist bias in the LS near the tropopause that is discussed in literature (e.g., Dyroff et al., 2014) is larger in subtropical and extratropical regions than in the tropics. In general, there is also a dry bias of the model in the UTLS that is of comparable size as the moist bias
- 560 – Similar to ERA–Interim, the operational analyses have the tendency to overestimate low water vapor mixing ratios in the LS and underestimate high mixing ratios in the UT. A case study of  $H_2O_{ANA}$  for a particular MACPEX flight in 2011 shows that the overestimation of water vapor near the flanks of the subtropical jet stream is reduced by a factor of two compared with  $H_2O_{ERA}$  (Fig. 4). Further, in the subtropical LS the underestimation of water vapor is
- 565 stronger for  $H_2O_{ERA}$  than for  $H_2O_{ANA}$ . This may well reflect the improvement of the model cycle used in 2011 for  $H_2O_{ANA}$  that benefits from several relevant changes compared to the model cycle used in 2007 for  $H_2O_{ERA}$ .
- In our study, the tropical troposphere and the extratropical UTLS turn out as atmospheric regions with challenging dynamics where both ERA–Interim and the operational analyses have
- 570 significant deviations from the observations. Anyhow, there is no clear difference between  $H_2O_{ERA}$  and  $H_2O_{ANA}$  in the UTLS during the entire period between 2001 and 2011. This suggests that problems remain concerning the data assimilation cycle and model resolution to accurately simulate the influence of atmospheric processes on the UTLS water vapor distribution. In particular, the influence of tropospheric processes is particularly challenging for the
- 575 assimilation system. These processes include deep convection, cloud microphysics and transport. Additionally, extratropical dynamical processes like mixing, cross-tropopause exchange and convective injections into the lower stratosphere (e.g., Schiller et al., 2009; Ravishankara, 2012; Ploeger et al., 2013) may affect the quality of ECMWF (re)analyses water vapor in the extratropical lower stratosphere. Dyroff et al. (2014) indicated an insufficient model res-
- 580 olution of small scale intrusions of air masses in the UTLS and an influence of numerical diffusion associated with the advection scheme in the vicinity of sharp humidity gradients at the tropopause may play a role. These issues may also be possible contributors to the model bias in the lower stratosphere (see also Stenke et al. (2008)).

The results of this study might be biased because of the different flight strategies of the campaigns included in the FISH based water vapor climatology. However, this study represents a comprehensive overview of the ECMWF water vapor distribution in the UTLS from the tropics toward the poles and a validation with independent observations. The results of this study are therefore particularly relevant for studies of the UTLS using ERA–Interim water vapor fields. These data have been frequently used for climatologies and trend studies over the past 30 years. Furthermore, the assessment of operational analyses of water vapor is valuable information for future developments of the ECMWF model and also as they are sometimes used as input data for numerical modeling of ice clouds. The correct simulation of the onset of ice nucleation and the prediction of ice clouds in the UT, e.g., based on coupled versions of Lagrangian and microphysical models, are particularly dependent on the quality of the input water vapor fields.

*Acknowledgements.* This analysis has been performed in memory of C. Schiller facilitating the ‘FISH–based water vapor climatology’ as developer and PI of the FISH instrument during his life’s work. A. Kunz has been supported by the European Union Seventh Framework Programme (FP7/2007-2013) under grant agreement no. 299666 with the Marie Curie Fellowship ‘Dynamical processes in the tropopause region and their impact on the distribution of atmospheric trace gases’ (PROTRO). Many thanks to the ECMWF for providing their products. We are also grateful to J.-U. Grooß, M. Krämer and P. Spichtinger for helpful discussions.

## References

- Andersson, E., Bauer, P., Beljaars, A., Chevallier, F., Hólm, E., Janisková, M., Kallberg, P., Kelly, G., Lopez, P., McNally, A., Moreau, E., Simmons, A. J., Thépaut, J.-N., and Tompkins, A. M., Assimilation and modeling of the atmospheric hydrological cycle in the ECMWF forecasting system, *Bull. Amer. Meteor. Soc.*, 86, 387-402. doi: <http://dx.doi.org/10.1175/BAMS-86-3-387>, 2005.
- Bechtold, P., Köhler, M., Jung, T., Doblas-Reyes, F., Leutbecher, M., Rodwell, M. J., Vitart, F., and Balsamo, G., Advances in simulating atmospheric variability with the ECMWF model: from synoptic to decadal timescales, *Q. J. R. Meteorol. Soc.*, 134, 1337-1351, 2008.
- Blom, C. E., Cortesi, U., and Redaelli, G., ENVISAT validation: Introduction to the correlative measurements by the chemistry payload on board the M-55 Geophysica, *Proc. of the 16th ESA Symposium on European Rocket and Balloon Programmes and Related Research*, St. Gallen, Switzerland, 2-5 June 2003 (ESA SP-530, August 2003).
- Cairo, F., Pommereau, J. P., Law, K. S., Schlager, H., Garnier, A., Fierli, F., Ern, M., Streibel, M., Arabas, S., Borrmann, S., Berthelier, J. J., Blom, C., Christensen, T., D'Amato, F., Di Donfrancesco, G., Deshler, T., Diedhiou, A., Durry, G., Engelsen, O., Goutail, F., Harris, N. R. P., Kerstel, E. R. T., Khaykin, S., Konopka, P., Kylling, A., Larsen, N., Lebel, T., Liu, X., MacKenzie, A. R., Nielsen, J., Oulanowski, A., Parker, D. J., Pelon, J., Polcher, J., Pyle, J. A., Ravegnani, F., Rivire, E. D., Robinson, A. D., Rckmann, T., Schiller, C., Simes, F., Stefanutti, L., Stroh, F., Some, L., Siegmund, P., Sitnikov, N., Vernier, J. P., Volk, C. M., Voigt, C., von Hobe, M., Viciani, S., and Yushkov, V., An introduction to the SCOUT-AMMA stratospheric aircraft, balloons and sondes campaign in West Africa, August 2006: rationale and roadmap, *Atmos. Chem. Phys.*, 10, 2237-2256, doi:10.5194/acp-10-2237-2010, 2010.
- Castanheira, J. M., Peevey, T. R., Marques, C. A. F., and Olsen, M. A., Relationships between Brewer-Dobson circulation, double tropopauses, ozone and stratospheric water vapour, *Atmos. Chem. Phys.*, 12, 10195-10208, doi:10.5194/acp-12-10195-2012, 2012.
- Dee, D. P., Uppala, S. M., Simmons, A. J., Berrisford, P., Poli, P., Kobayashi, S., Andrea, U., Balmaseda, M. A., Balsamo, G., Bauer, P., Bechtold, P., Beljaars, A. C. M., von de Berg, L., Bidlot, J., Bormann, N., Delsol, C., Dragani, R., Fuentes, M., Geer, A. J., Haimberger, L., Healy, S. B., Hersbach, H., Hólm, E. V., Isaksen, I., Kallberg, P., Köhler, M., Matricardi, M., McNally, A. P., Monge-Sanz, B. M., Morcrette, J.-J., Park, B.-K., Peubey, C., de Rosnay, P., Tavolato, C., Thépaut, J.-N., and Vitart, F., The ERA-Interim reanalysis: configuration and performance of the data assimilation system, *Q. J. R. Meteorol. Soc.*, 137, 553-597, DOI:10.1002/qj.828, 2011.
- Dyroff, C., Zahn, A., Christner, E., Forbes, R. M., Tompkins, A. M., and van Velthoven, P. F. J., Comparison of ECMWF analysis and forecast humidity data to CARIBIC upper troposphere and lower stratosphere observations, *Q. J. R. Meteorol. Soc.*, in review, 2014.
- Engel, A., Bönisch, H., Brunner, D., Fischer, H., Franke, H., Günther, G., Gurk, C., Hegglin, M., Hoor, P., Königstedt, R., Krebsbach, M., Maser, R., Parchatka, U., Peter, T., Schell, D., Schiller, C., Schmidt, U., Spelten, N., Szabo, T., Weers, U., Wernli, H., Wetter, T., and Wirth, V., Highly resolved observations of trace gases in the lowermost stratosphere and upper troposphere from the SPURT project: an overview, *Atmos. Chem. Phys.*, 6, 283-301, doi:10.5194/acp-6-283-2006, 2006.
- Flentje, H., Dörnbrack, A., Fix, A., Ehret, G., and Hólm, E., Evaluation of ECMWF water vapour fields by

- airborne differential absorption lidar measurements: a case study between Brazil and Europe, *Atmos. Chem. Phys.*, 7, 5033-5042, doi:10.5194/acp-7-5033-2007, 2007.
- Forbes, R., Tompkins, A. M., and Untch, A., A new prognostic bulk microphysics scheme for the IFS, ECMWF Technical Memoranda No. 649., 2011. (available from <http://www.ecmwf.int/>)
- 645 Forster, P. M. de F. and Shine, K. P., Radiative forcing and temperature trends from stratospheric ozone changes, *J. Geophys. Res.*, 102(D9), 10841–10855, 1997.
- Fueglistaler, S., Dessler, A. E., Dunkerton, T. J., Folkins, I., Fu, Q. and Mote, P. W., Tropical tropopause layer, *Rev. Geophys.*, 47, RG1004, doi:10.1029/2008RG000267, 2009.
- Haynes, P. and Shuckburgh, E., Effective diffusivity as a diagnostic of atmospheric transport 2. Troposphere  
650 and lower stratosphere, *J. Geophys. Res.*, 105, D18, 22,795–22,810, 2000.
- Hólm, E., Revision of the ECMWF humidity analysis: Construction of a Gaussian control variable, Proceedings of the ECMWF/GEWEX Workshop on Humidity Analysis, 8-11 July 2002, ECMWF Reading, UK, 2002.
- Jensen, E. and Pfister, L., Transport and freeze-drying in the tropical tropopause layer, *J. Geophys. Res.*, 109, D02207, doi:10.1029/2003JD004022, 2004.
- 655 Jones, R. L., and Pyle, J. A., Observations of CH<sub>4</sub> and N<sub>2</sub>O by the NIMBUS 7 SAMS: A comparison with in situ data and two-dimensional numerical model calculations, *J. Geophys. Res.*, 89, 3D1644, doi:10.1029/JD089iD04p05263, 1984.
- Köhler, M., Ahlgrimm, M., Beljaars, A. C. M., Unified treatment of dry convective and stratocumulus-topped boundary layers in the ECMWF model, *Q. J. R. Meteorol. Soc.*, 137, 43–57, 2011.
- 660 Kunz, A., Schiller, C., Rohrer, F., Smit, H. G. J., Nedelec, P., and Spelten, N., Statistical analysis of water vapour and ozone in the UT/LS observed during SPURT and MOZAIC, *Atmos. Chem. Phys.*, 8, 6603-6615, doi:10.5194/acp-8-6603-2008, 2008.
- Kunz, A., Konopka, P., Müller, R., and Pan, L. L., Dynamical tropopause based on isentropic potential vorticity gradients, *J. Geophys. Res.*, 116, D01110, doi:10.1029/2010JD014343, 2011a.
- 665 Kunz, A., Pan, L. L., Konopka, P., Kinnison, D. E., and Tilmes, S., Chemical and dynamical discontinuity at the extra-tropical tropopause-based on START08 and WACCM analyses, *J. Geophys. Res.*, 116, D24302, doi:10.1029/2011JD016686, 2011b.
- Kunz, A., Müller, R., Homonnai, V., Jánosi, I. M., Hurst, D., Rap, A., Forster, P. M., Rohrer, F., Spelten, N., and Riese, M., Extending water vapor trend observations over Boulder into the tropopause region: trend  
670 uncertainties and resulting radiative forcing, *J. Geophys. Res.*, 118, 11,269-11,284, doi:10.1002/jgrd.50831, 2013.
- Lamquin, N., Gierens, K., Stubenrauch, C. J., and Chatterjee, R., Evaluation of upper tropospheric humidity forecasts from ECMWF using AIRS and CALIPSO data, *Atmos. Chem. Phys.*, 9, 1779-1793, doi:10.5194/acp-9-1779-2009, 2009.
- 675 Luo, Z., Kley, D., Johnson, R. H., and Smit, H., Ten Years of Measurements of Tropical Upper-Tropospheric Water Vapor by MOZAIC. Part II: Assessing the ECMWF Humidity Analysis, *J. Climate*, 21, DOI: 10.1175/2007JCLI1887.1, 2007.
- McKenna, D., S., Konopka, P., Grooß, J., U., Günther, G., and R. Müller, A new Chemical Lagrangian Model of the Stratosphere (CLaMS), 1. Formulation of advection and mixing, *J. Geophys. Res.*, 107, NO. D16, 4309, doi:10.1029/2000JD000114, 2002.
- 680

- Oikonomou, E. K., and O'Neill, A., Evaluation of ozone and water vapor fields from the ECMWF reanalysis ERA-40 during 1991-1999 in comparison with UARS satellite and MOZAIC aircraft observations, *J. Geophys. Res.*, 111, D14109, doi:10.1029/2004JD005341, 2006.
- 685 Olsen, M. A., Douglas, A. R., Schoeberl, M. R., Rodriguez, J. M., and Yoshida, Y., Interannual variability of ozone in the winter lower stratosphere and the relationship to lamina and irreversible transport, *J. Geophys. Res.*, 115, D15305, doi:10.1029/2009JD013004, 2010.
- Pan, L. L., Randel, W. J., Gary, B. L., Mahoney, M. J., and Hints, E. J., Definition and sharpness of the extratropical tropopause: A trace gas perspective, *J. Geophys. Res.*, 109, D23103, doi:10.1029/2004JD004982, 2004.
- 690 Pan, L. L., Kunz, A., Homeyer, C. R., Munchak, L. A., Kinnison, D. E., and Tilmes, S., Commentary on using equivalent latitude in the upper troposphere and lower stratosphere, *Atmos. Chem. Phys.*, 12, 9187-9199, doi:10.5194/acp-12-9187-2012, 2012.
- Ploeger, F., Günther, G., Konopka, P., Fueglistaler, S., Müller, R., Hoppe, C., Kunz, A., Spang, R., Groö, J.-U., and Riese, M., Horizontal water vapor transport in the lower stratosphere from subtropics to high latitudes during boreal summer, *J. Geophys. Res.*, 118, 1-17, doi:10.1002/jgrd.50636, 2013.
- 695 Ravishankara, A. R., Water vapor in the lower stratosphere, *Science*, 337, 809-810, 2012.
- Riese, M., Ploeger, F., Rap, A., Vogel, B., Konopka, P., Dameris, M., and Forster, P., Impact of uncertainties in atmospheric mixing on simulated UTLS composition and related radiative effects, *J. Geophys. Res.*, 117, doi:10.1029/2012JD017751, D16305, 2012.
- 700 Röckmann, T., Groö, J.-U., and Müller, R., The impact of anthropogenic chlorine emissions, stratospheric ozone change and chemical feedbacks on stratospheric water, *Atmos. Chem. Phys.*, 4, 693-699, 2004.
- Rohrer, F., and Berresheim, H., Strong correlation between levels of tropospheric hydroxyl radicals and solar ultraviolet radiation, *Nature*, 442, 184-187, 2006.
- Rohs, S., Schiller, C., Riese, M., Engel, A., Schmidt, U., Wetter, T., Levin, I., Nakazawa, T., and Aoki, S., Long-term changes of methane and hydrogen in the stratosphere in the period 1978-2003 and their impact on the abundance of stratospheric water vapor, *J. Geophys. Res.*, 111, doi:10.1029/2005JD006877, D14315, 2006.
- 705 Schiller, C., Groö, J.-U., Konopka, P., Plöger, F., Silva dos Santos, F. H., and Spelten, N., Hydration and dehydration at the tropical tropopause, *Atmos. Chem. Phys.*, 9, 9647-9660, 2009.
- 710 Schäfler, A., Dörnbrack, A., Kiemle, C., Rahm, S., and Wirth, M., Tropospheric water vapor transport as determined from airborne lidar measurements, *J. Atmos. Ocean. Techn.*, 2017-2030, doi:10.1175/2010JTECHA1418.1, 2010.
- Solomon, S., Rosenlof, K. H., Portman, R. W., Daniel, J. S., Davis, S. M., Sanford, F. J., and Plattner, G.-K., Contributions of stratospheric water vapor to decadal changes in the rate of global warming, *Science*, 327, 1219-1223, 2010.
- 715 Stenke, A., Grewe, V., and Ponater, M., Lagrangian transport of water vapor and cloud water in the ECHAM4 GCM and its impact on the cold bias, *Clim. Dyn.*, 31, 491-506, 2008.
- Tilmes, S., Pan, L. L., Hoor, P., Atlas, E., Avery, M. A., Campos, T., Christensen, L. E., Diskin, G. S., Gao, R.-S., Herman, R. L., Hints, E. J., Loewenstein, M., Lopez, J., Paige, M. E., Pittman, J. V., Podolske, J. R., Proffitt, M. R., Sachse, G. W., Schiller, C., Schlager, H., Smith, J., Spelten, N., Webster, C., Weinheimer, A.,
- 720

- and Zondlo, M. A., An aircraft-based upper troposphere lower stratosphere O<sub>3</sub>, CO, and H<sub>2</sub>O climatology for the Northern Hemisphere, *J. Geophys. Res.*, 115, D14303, doi:10.1029/2009JD012731, 2010.
- Tompkins, A. M., Gierens, K., and Rädcl, G., Ice supersaturation in the ECMWF integrated forecast system, *Q. J. R. Meteorol. Soc.*, 133, 53–63, DOI: 10.1002/qj.14, 2007.
- 725 Uppala, S. M., et al., The ERA-40 reanalysis, *Q. J. R. Meteorol. Soc.*, 131, 612, 2961–3012, DOI: 10.1256/qj.04.176, 2006.
- Vaughan, G., Schiller, C., MacKenzie, A. R., Bower, K., Peter, T., Schlager, H., Harris, N. R. P., and May, P. T.E., SCOUT-O3/ACTIVE High-altitude aircraft measurements around deep tropical convection, *BAMS*, 89, 647–662, 10.1175/BAMS-89-5-647, 2008.
- 730 von Hobe, M., Bekki, S., Borrmann, S., Cairo, F., D’Amato, F., Di Donfrancesco, G., Dörnbrack, A., Ebersoldt, A., Ebert, M., Emde, C., Engel, I., Ern, M., Frey, W., Griessbach, S., Grooß J.-U., Gulde, T., Günther, G., Hösen, E., Hoffmann, L., Homonnai, V., Hoyle, C. R., Isaksen, I. S. A., Jackson, D. R., Jánosi, I. M., Kandler, K., Kalicinsky, C., Keil, A., Khaykin, S. M., Khosrawi, F., Kivi, R., Kuttippurath, J., Laube, J. C., Lefèvre, F., Lehmann, R., Ludmann, S., Luo, B. P., Marchand, M., Meyer, J., Mitev, V., Molleker, S., Müller,
- 735 R., Oelhaf, H., Olschewski, F., Orsolini, Y., Peter, T., Pfeilsticker, K., Piesch, C., Pitts, M. C., Poole, L. R., Pope, F. D., Ravegnani, F., Rex, M., Riese, M., Röckmann, T., Rognerud, B., Roiger, A., Rolf, C., Santee, M. L., Scheibe, M., Schiller, C., Schlager, H., Siciliani de Cumis, M., Sitnikov, N., Søvde, O. A., Spang, R., Spelten, N., Stordal, F., Sumińska-Ebersoldt, O., Viciani, S., Volk, C. M., vom Scheidt, M., Ulanovski, A., von der Gathen, P., Walker, K., Wegner, T., Weigel, R., Weinbuch, S., Wetzel, G., Wienhold, F. G., Wintel,
- 740 J., Wohltmann, I., Woiwode, W., Young, I. A. K., Yushkov, V., Zobrist, B., and Stroh, F., Reconciliation of essential process parameters for an enhanced predictability of Arctic stratospheric ozone loss and its climate interactions, *Atmos. Chem. Phys.*, 12, 30661-30754, doi:10.5194/acpd-12-30661-2012, 2013.
- World Meteorological Organization (1957), *Meteorology—A three-dimensional science*, *WMO Bull* (6), 134–138.
- 745 Zöger, M., Afchine, A., Eicke, N., Gerhards, M.-T., Klein, E., McKenna, D. S., Mörschel, U., Schmidt, U., Tan, V., Tuitjer, F., Woyke, T., and Schiller, C., Fast in-situ stratospheric hygrometers: A new family of balloon-borne and airborne Lyman  $\alpha$  photofragment fluorescence hygrometers, *J. Geophys. Res.*, 104, 1807-1816, 1999.

## Tables

**Table 1.** Information on campaigns of the FISH-based water vapor climatology including both local and transfer flights. The number of missions refer to the flight missions used for this climatology, i.e., the total amount of flight missions per campaign may be higher. The approximate regional extent of the 148 flight missions is shown in Fig. 1.

Campaign	Time	Location	Flight missions	Flight hours	Campaign objectives
<b>SPURT</b> (Trace gas transport in the tropopause region) e.g. Engel et al. (2006)	11/2001, 01/2002 05/2002, 08/2002 10/2002, 02/2003 04/2003, 07/2003	Hohn (Germany)	34	≈147	UTLS trace gas climatology Atmospheric transport and seasonal variation of trace gases
<b>EUPLEX</b> (European Polar Stratospheric Cloud and Lee Wave Experiment)	01/2003, 02/2003	Kiruna (Sweden)	7	≈40	Polar Stratospheric Clouds Ozon loss in polar vortex Chlorine activation De- and Renitrification
<b>POLARCAT GRACE</b> (Greenland Aerosol and Chemistry Experiment) <a href="http://www.pa.op.dlr.de/polarcat/">www.pa.op.dlr.de/polarcat/</a>	07/2008	Kangerlussuaq (Greenland)	13	≈80	Boreal forest fire emissions into the UTLS Annual variation of trace gases and aerosols in the Arctic
<b>RECONCILE</b> (Reconciliation of essential process parameters for an enhanced predictability of arctic strat. ozone loss and its climate interactions) e.g. von Hobe et al. (2013)	01/2010, 02/2010 03/2010	Kiruna (Sweden)	13	≈52	Polar vortex chemical reactions Catalytic CLOx/BrOx chemistry Chlorine activation on PSCs NAT nucleation mechanisms
<b>ENVISAT</b> e.g. Blom et al. (2003)	06/2002, 10/2002  03/2003	Forli (Italy) & Kiruna (Sweden)	10  5	≈44  ≈20	Validation of ENVISAT chemistry instruments at midlatitudes  ENVISAT validation in the Arctic
<b>CIRRUS</b>	12/2003, 11/2004 11/2006	Hohn (Germany)	12	≈52	Cirrus formation mechanism and radiative effects Chemical and microphysical properties of cloud particles
<b>MACPEX</b> (Midlatitude Airborne Cirrus Properties Experiment) <a href="http://www.espo.nasa.gov/macpex/">www.espo.nasa.gov/macpex/</a>	04/2011	Houston (USA,TX)	15	≈100	Cirrus formation mechanism H <sub>2</sub> O instrumental inter-comparison
<b>TROCCINOX</b> (Tropical Convection, Cirrus, and Nitrogen Oxides Experiment) <a href="http://www.pa.op.dlr.de/troccinox">www.pa.op.dlr.de/troccinox</a>	01/2005, 02/2005	Aracatuba (Brazil)	14	≈64	Impact of tropical convection on UTLS trace gases and particles Lightning produced NO <sub>x</sub> in tropical thunderstorms
<b>SCOUT</b> (Stratospheric–Climate Links with Emphasis on the Upper Troposphere and Lower Stratosphere) e.g. Vaughan et al. (2008)	11/2005, 12/2005	Darwin (Australia)	16	≈88	Deep tropical convection Composition of the Tropical Transition Layer Transport of trace gases into the tropical UTLS
<b>AMMA</b> (African Monsoon Multidisciplinary Analysis) e.g. Cairo et al. (2010)	07/2006, 08/2006	Ouagadougou (Burkina Faso)	9	≈40	Intense mesoscale convection connected with African monsoon Large scale transport into the UTLS Lightning and NO <sub>x</sub> production

## Figure Captions

**Fig. 1.** Latitude–longitude (panel a) and altitude–latitude (panel b) representation of FISH water vapor measurements. Counts of 1 Hz measurements are shown for  $5^\circ \text{ lat} \times 5^\circ \text{ lon}$  and  $1\text{ km} \times 5^\circ \text{ lat}$  bins, respectively. The measurement locations of the different campaigns are indicated in both panels. The ERA–Interim horizontal wind speed (20 m/s and 30 m/s) at 13 km (panel a) and the zonal wind speed (10 m/s, 20 m/s, 30 m/s, 40 m/s) as cross–section through all altitudes (panel b) are shown as mean over all 136 flight mission days between 2001 and 2011. The mean ERA–Interim isentropic surfaces (290 K, 320 K, 350 K, 380 K, and 410 K) are black dashed lines, and the mean location of the thermal tropopause is given by a white solid line.

**Fig. 2.** Relationship between the asymmetric quantity  $\Delta\text{H}_2\text{O}$  and the symmetric quantity  $\Delta\text{H}_2\text{O}^{\log 2}$  (black line) that is used for the evaluation of simulated and observed water vapor fields. Overestimations ( $\Delta\text{H}_2\text{O}^{\log 2} > 0$ ) are indicated by red dots, underestimations ( $\Delta\text{H}_2\text{O}^{\log 2} < 0$ ) by blue dots, and a perfect relationship ( $\Delta\text{H}_2\text{O}^{\log 2} = 0$ ) by the green dot. The values presented are the most relevant ones used in the investigation. In particular,  $\Delta\text{H}_2\text{O}^{\log 2}$  values of 1, 1.6, 2, 2.3, 2.6, 2.8, 3.0, 3.2, and 3.3 correspond to a model water vapor that is two, three, four, five, six, seven, eight, nine, and ten times larger than the observed water vapor.

**Fig. 3.** Example flight on 1 April 2011 during the MACPEX campaign over the U.S. between  $15 - 40^\circ \text{ N}$ . Panel a: Altitude–time projection of ERA–Interim static stability (colored contours) along the flight path (blue solid line). Isentropes (320K, 350K, 380K, and 410K) as black dashed lines, zonal wind speed as orange lines (30 m/s and 40 m/s), and thermal tropopause as white line. Panel b: Water vapor mixing ratio in ppmv measured by FISH ( $\text{H}_2\text{O}_{\text{FISH}}$ , black line) and ECMWF reanalysis ( $\text{H}_2\text{O}_{\text{ERA}}$ , orange line) and operational analysis water vapor mixing ratio ( $\text{H}_2\text{O}_{\text{ANA}}$ , green line). Panel c: Latitude–longitude position of the flight path (blue solid line). Start position of the flight (read point) and the horizontal wind speed (gray contours) are highlighted.

**Fig. 4.** Panel a: The ratio  $\Delta\text{H}_2\text{O}^{\log 2}$  for the reanalysis (orange line) and the operational analysis water vapor (green line) for the example MACPEX flight on 1 April 2011 shown in Fig. 3. The red solid line marks a perfect agreement ( $\Delta\text{H}_2\text{O}^{\log 2} = 0$ ). The red dashed lines indicate the limits when the simulations are twice ( $\Delta\text{H}_2\text{O}^{\log 2} = 1$ ) or half ( $\Delta\text{H}_2\text{O}^{\log 2} = -1$ ) as high as the observations. Panel b: Mean water vapor mixing ratio per  $\Delta\text{H}_2\text{O}_{\text{ERA}}^{\log 2}$  bin of  $\text{H}_2\text{O}_{\text{FISH}}$  (black line) and  $\text{H}_2\text{O}_{\text{ERA}}$  (orange line). Panel c: Mean water vapor mixing ratio of  $\Delta\text{H}_2\text{O}_{\text{ANA}}^{\log 2}$  bin for  $\text{H}_2\text{O}_{\text{FISH}}$  (black line) and  $\text{H}_2\text{O}_{\text{ANA}}$  (green line).

**Fig. 5.** Left panels: Frequency distribution of  $\Delta\text{H}_2\text{O}_{\text{ERA}}^{\log 2}$  separately for each measurement campaign. Bin size of  $\Delta\text{H}_2\text{O}_{\text{ERA}}^{\log 2}$  is organized according to Fig. 2. Only frequencies larger than 0.1 % are shown. The red solid line marks a perfect agreement ( $\Delta(\text{H}_2\text{O}_{\text{ERA}}^{\log 2}) = 0$ ). The mean of the distribution (green solid line), the median (green dashed line), and the standard deviation (blue dashed line) are also shown. Right panels: Mean water vapor mixing ratio per  $\Delta\text{H}_2\text{O}_{\text{ERA}}^{\log 2}$  bin for  $\text{H}_2\text{O}_{\text{FISH}}$  (black line) and  $\text{H}_2\text{O}_{\text{ERA}}$  (orange line).



**Fig. 6.** Counts of data, potential temperature, and water vapor for all measurement campaigns shown in Fig. 1 plotted in a  $\Delta H_2O_{ERA}^{\log 2}$  and thermal tropopause related coordinate system. The distributions are shown for the tropical domain ( $z_{TP} > 14$  km) (panels a, b, and c), the subtropical ( $12 \text{ km} \leq z_{TP} \leq 14 \text{ km}$ ) (panels d, e, and f), and for the extratropical domain ( $z_{TP} < 12 \text{ km}$ ) (panels g, h, and i). The red solid line marks a perfect agreement, i.e.,  $\Delta(H_2O_{ERA}^{\log 2}) = 0$ , and the red dashed lines mark a ratio  $\Delta H_2O_{ERA}^{\log 2}$  between -2 and 2. Thermal tropopause bin size is 1 km and  $\Delta H_2O_{ERA}^{\log 2}$  bins are organized as for Fig. 5

**Fig. 7.** Correlation between  $H_2O_{ERA}$  and  $H_2O_{FISH}$  for the tropical domain (panel a), subtropical (panel b) and extratropical domain (panel c). Filled gray contours represent the counts of data within logarithmic  $H_2O$  bins. Red lines mark selected  $\Delta H_2O_{ERA}^{\log 2}$  ratios and the white lines surround bins that are representative for the stratosphere.

**Fig. 8.** Counts of data (panel a), mean  $\Delta H_2O_{ERA}^{\log 2}$  (panel b) and mean  $H_2O_{FISH}$  (panel c) based on all Northern hemisphere measurement campaigns (TROCCINOX and SCOUT are excluded) per 5 K potential temperature and  $5^\circ$  equivalent latitude bin. The equivalent latitude position of the dynamic tropopause (white circles) is shown on each isentrope as mean over all measurement days. Zonal mean zonal wind speed at all measurement days is represented by orange contours.

**Fig. 9.** Counts of data (panel a), mean potential temperature (panel b) and mean  $H_2O_{FISH}$  (panel c) of all Northern hemisphere measurement campaigns (TROCCINOX and SCOUT are excluded) plotted as averages per logarithmic  $\Delta H_2O_{ERA}^{\log 2}$  and  $5^\circ$  relative equivalent latitude difference bin with respect to the dynamic tropopause (see white circles in Fig. 8).

**Fig. 10.** Left panels: Daily mean  $\Delta H_2O^{\log 2}$  of operational analysis water vapor mixing ratio ( $H_2O_{ANA}$ , black-orange dots) over the time for stratospheric measurements in the tropical (panel a), subtropical (panel d), and extratropical domain (panel g). The range between the minimum and maximum value of  $\Delta H_2O_{ANA}^{\log 2}$  on each day is marked by the orange vertical bars, the daily mean  $\Delta H_2O_{ERA}^{\log 2}$  by the black-green dots. Dashed red lines indicate  $\Delta H_2O^{\log 2}$  between -3.32 and 3.32, black dashed lines indicate the dates when selected IFS cycles became operational. Right panels: Correlation of  $H_2O_{FISH}$  with  $H_2O_{ANA}$  (orange) and with  $H_2O_{ERA}$  (green) for two IFS cycle time periods (gray shadings, left panels). The first period, i.e., IFS cycles 28r1-31r1, include measurements from 09 March 2004 to 12 September 2006 (panels b, e, and h) and the second period, i.e., IFS cycles 36r1-37r2, measurements from 26 January 2010 to 18 May 2011 (panels c, f, and i). Means per  $H_2O_{FISH}$  bin are shown by black-surrounded larger dots.

**Fig. 11.** As Figure 10 but for tropospheric measurements in the three different atmospheric domains.

**Fig. 12.** Same as Fig. 3 but for a special flight segment during the MACPEX flight on 11 April 2011.

## Figures

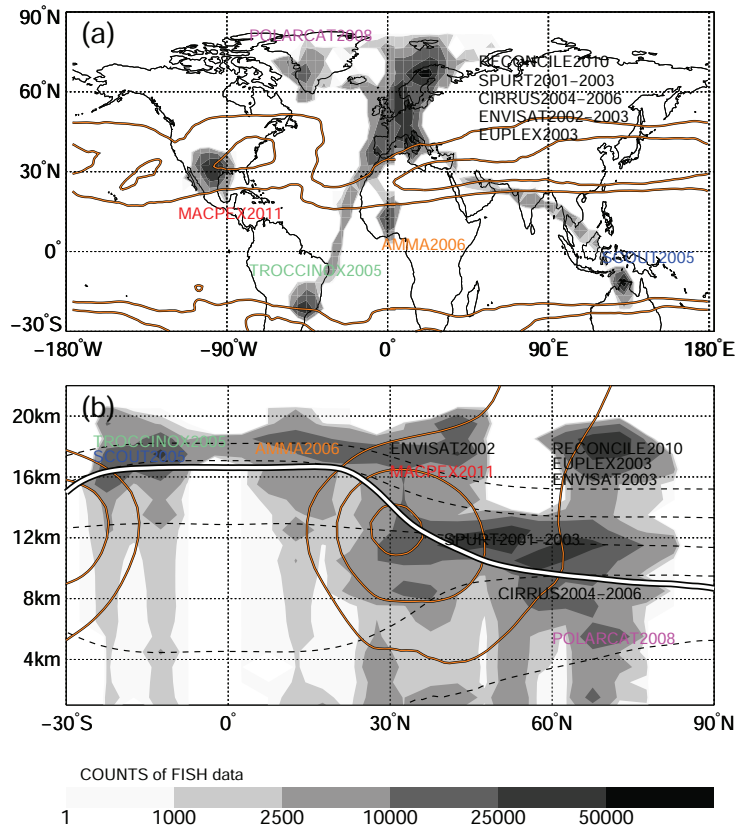


**Fig. 1.** Latitude–longitude (panel a) and altitude–latitude (panel b) representation of FISH water vapor measurements. Counts of 1 Hz measurements are shown for  $5^\circ \text{ lat} \times 5^\circ \text{ lon}$  and  $1\text{ km} \times 5^\circ \text{ lat}$  bins, respectively. The measurement locations of the different campaigns are indicated in both panels. The ERA–Interim horizontal wind speed (20 m/s and 30 m/s) at 13 km (panel a) and the zonal wind speed (10 m/s, 20 m/s, 30 m/s, 40 m/s) as cross-section through all altitudes (panel b) are shown as mean over all 136 flight mission days between 2001 and 2011. The mean ERA–Interim isentropic surfaces (290 K, 320 K, 350 K, 380 K, and 410 K) are black dashed lines, and the mean location of the thermal tropopause is given by a white solid line.

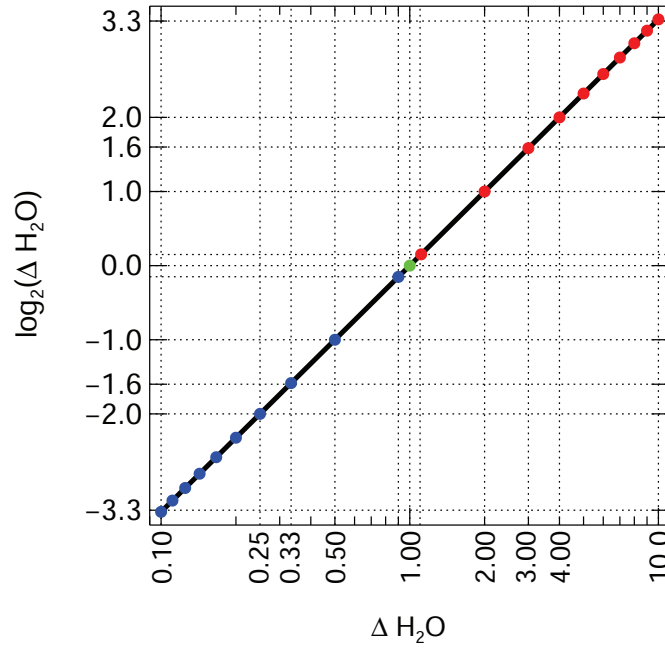


**Fig. 2.** Relationship between the asymmetric quantity  $\Delta H_2O$  and the symmetric quantity  $\Delta H_2O^{\log_2}$  (black line) that is used for the evaluation of simulated and observed water vapor fields. Overestimations ( $\Delta H_2O^{\log_2} > 0$ ) are indicated by red dots, underestimations ( $\Delta H_2O^{\log_2} < 0$ ) by blue dots, and a perfect relationship ( $\Delta H_2O^{\log_2} = 0$ ) by the green dot. The values presented are the most relevant ones used in the investigation. In particular,  $\Delta H_2O^{\log_2}$  values of 1, 1.6, 2, 2.3, 2.6, 2.8, 3.0, 3.2, and 3.3 correspond to a model water vapor that is two, three, four, five, six, seven, eight, nine, and ten times larger than the observed water vapor.

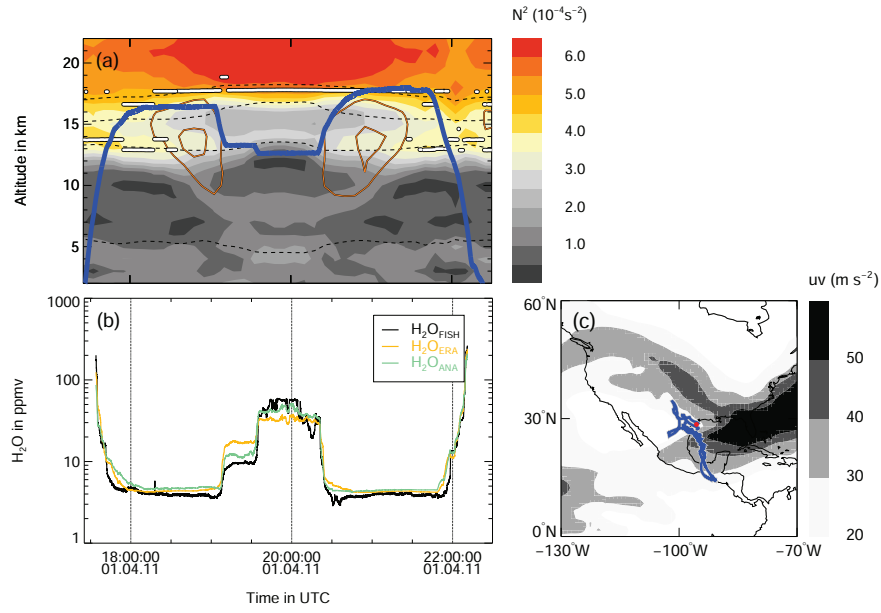


**Fig. 3.** Example flight on 1 April 2011 during the MACPEX campaign over the U.S. between  $15 - 40^\circ \text{ N}$ . Panel a: Altitude–time projection of ERA–Interim static stability (colored contours) along the flight path (blue solid line). Isentropes (320K, 350K, 380K, and 410K) as black dashed lines, zonal wind speed as orange lines (30 m/s and 40 m/s), and thermal tropopause as white line. Panel b: Water vapor mixing ratio in ppmv measured by FISH ( $\text{H}_2\text{O}_{\text{FISH}}$ , black line) and ECMWF reanalysis ( $\text{H}_2\text{O}_{\text{ERA}}$ , orange line) and operational analysis water vapor mixing ratio ( $\text{H}_2\text{O}_{\text{ANA}}$ , green line). Panel c: Latitude–longitude position of the flight path (blue solid line). Start position of the flight (read point) and the horizontal wind speed (gray contours) are highlighted.

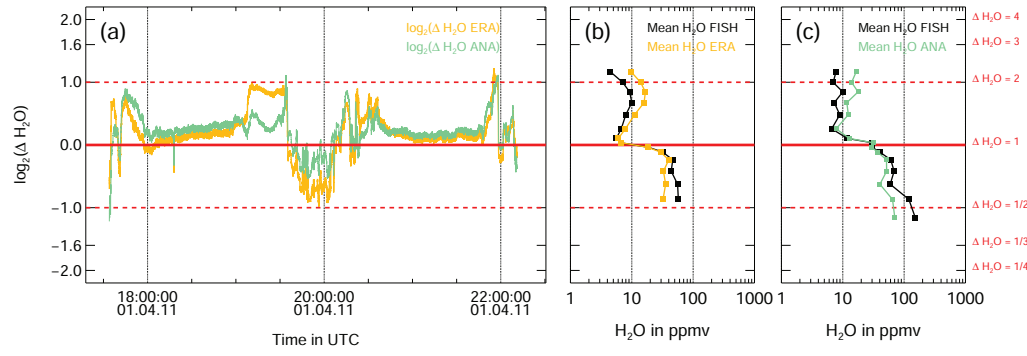


**Fig. 4.** Panel a: The ratio  $\Delta H_2O^{\log^2}$  for the reanalysis (orange line) and the operational analysis water vapor (green line) for the example MACPEX flight on 1 April 2011 shown in Fig. 3. The red solid line marks a perfect agreement ( $\Delta H_2O^{\log^2} = 0$ ). The red dashed lines indicate the limits when the simulations are twice ( $\Delta H_2O^{\log^2} = 1$ ) or half ( $\Delta H_2O^{\log^2} = -1$ ) as high as the observations. **Panel b:** Mean water vapor mixing ratio per  $\Delta H_2O_{ERA}^{\log^2}$  bin of  $H_2O_{FISH}$  (black line) and  $H_2O_{ERA}$  (orange line). **Panel c:** Mean water vapor mixing ratio of  $\Delta H_2O_{ANA}^{\log^2}$  bin for  $H_2O_{FISH}$  (black line) and  $H_2O_{ANA}$  (green line).

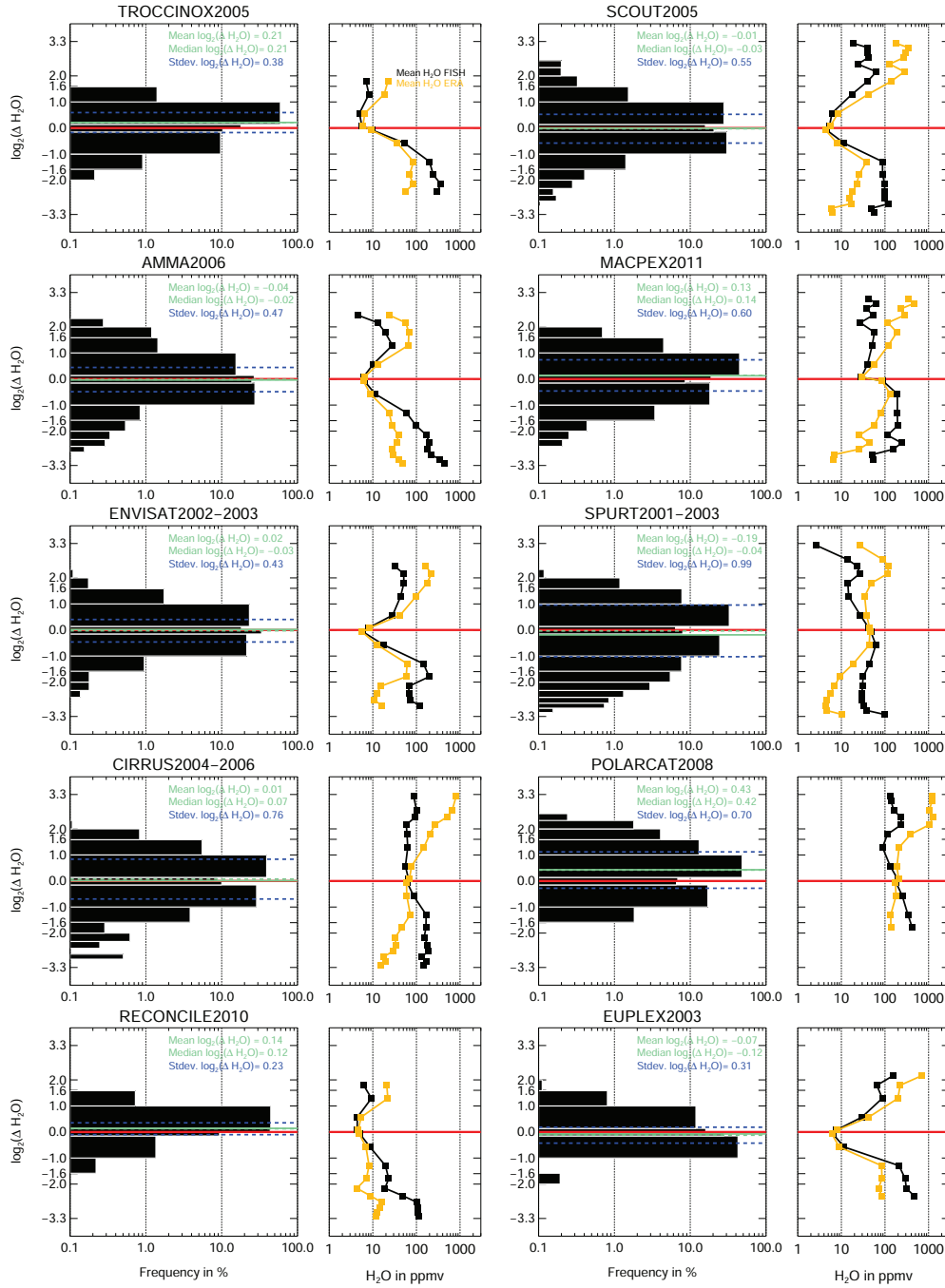


**Fig. 5.** Left panels: Frequency distribution of  $\Delta H_2O_{ERA}^{\log_2}$  separately for each measurement campaign. Bin size of  $\Delta H_2O_{ERA}^{\log_2}$  is organized according to Fig. 2. Only frequencies larger than 0.1 % are shown. The red solid line marks a perfect agreement ( $\Delta(H_2O_{ERA}^{\log_2}) = 0$ ). The mean of the distribution (green solid line), the median (green dashed line), and the standard deviation (blue dashed line) are also shown. Right panels: Mean water vapor mixing ratio per  $\Delta H_2O_{ERA}^{\log_2}$  bin for  $H_2O_{FISH}$  (black line) and  $H_2O_{ERA}$  (orange line).

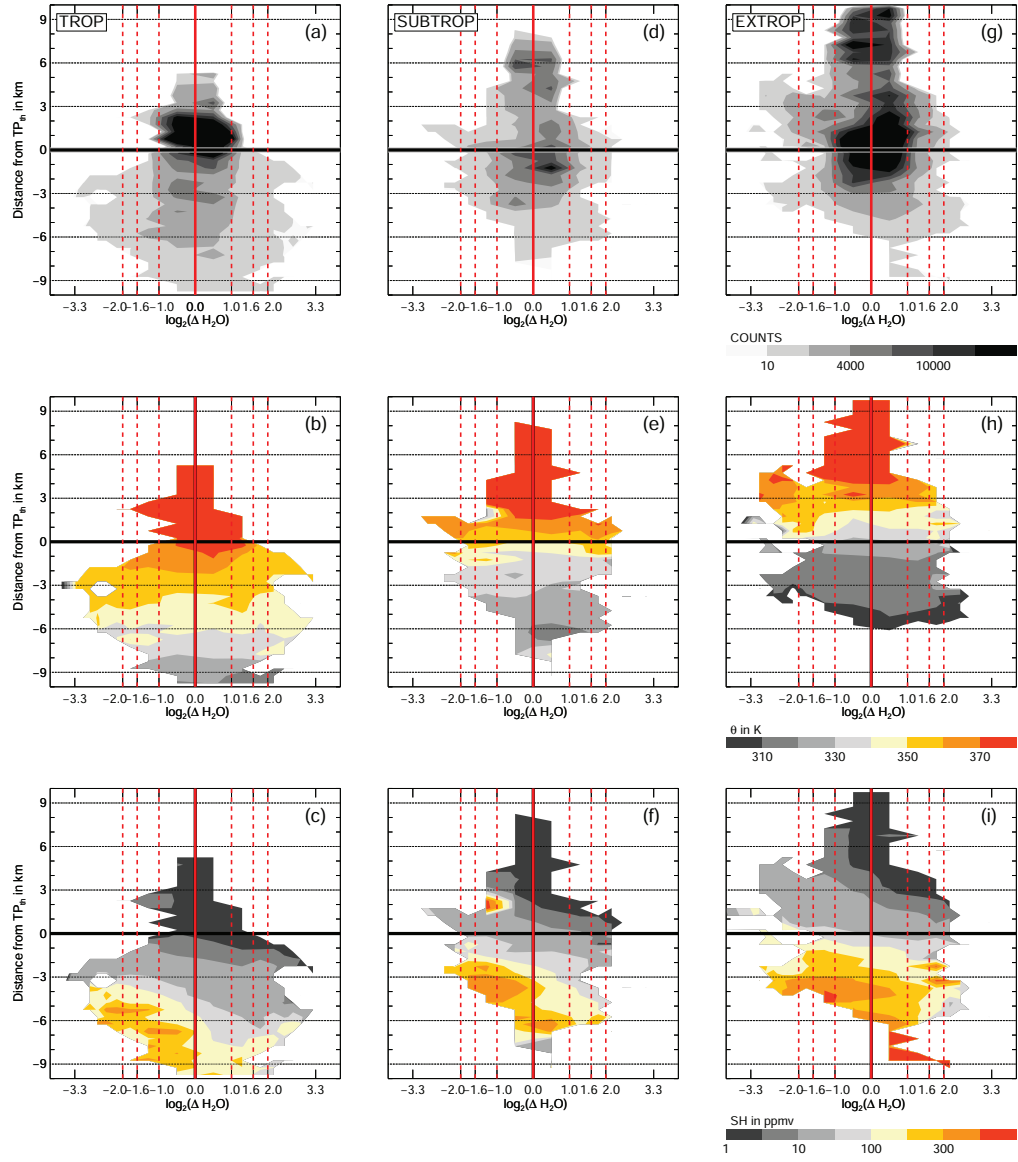


**Fig. 6.** Counts of data, potential temperature, and water vapor for all measurement campaigns shown in Fig. 1 plotted in a  $\Delta H_2O_{\text{ERA}}^{\log 2}$  and thermal tropopause related coordinate system. The distributions are shown for the tropical domain ( $z_{\text{TP}} > 14$  km) (panels a, b, and c), the subtropical ( $12 \text{ km} \leq z_{\text{TP}} \leq 14$  km) (panels d, e, and f), and for the extratropical domain ( $z_{\text{TP}} < 12$  km) (panels g, h, and i). The red solid line marks a perfect agreement, i.e.,  $\Delta(H_2O_{\text{ERA}}^{\log 2}) = 0$ , and the red dashed lines mark a ratio  $\Delta H_2O_{\text{ERA}}^{\log 2}$  between -2 and 2. Thermal tropopause bin size is 1 km and  $\Delta H_2O_{\text{ERA}}^{\log 2}$  bins are organized as for Fig. 5

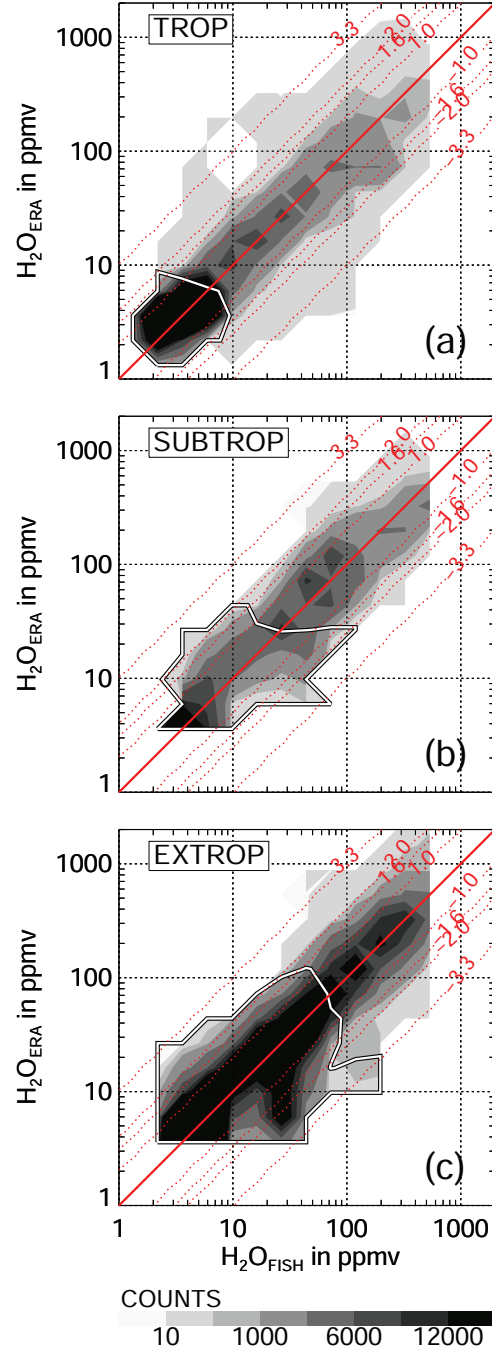


**Fig. 7.** Correlation between  $\text{H}_2\text{O}_{\text{ERA}}$  and  $\text{H}_2\text{O}_{\text{FISH}}$  for the tropical domain (panel a), subtropical (panel b) and extratropical domain (panel c). Filled gray contours represent the counts of data within logarithmic  $\text{H}_2\text{O}$  bins. Red lines mark selected  $\Delta\text{H}_2\text{O}_{\text{ERA}}^{\log 2}$  ratios and the white lines surround bins that are representative for the stratosphere.



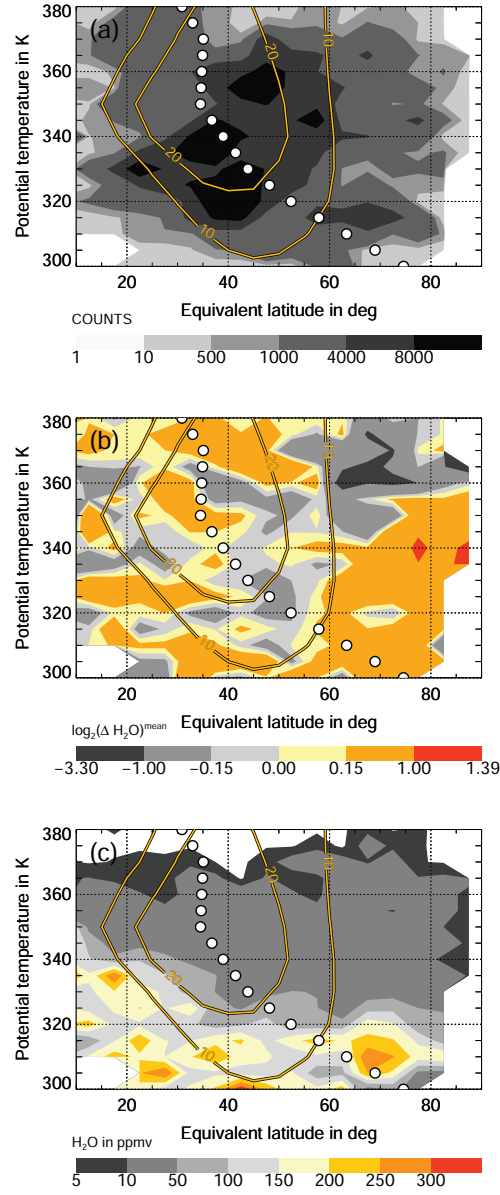


**Fig. 8.** Counts of data (panel a), mean  $\Delta H_2O_{\text{ERA}}^{\log_2}$  (panel b) and mean  $H_2O_{\text{FISH}}$  (panel c) based on all Northern hemisphere measurement campaigns (TROCCINOX and SCOUT are excluded) per 5 K potential temperature and  $5^\circ$  equivalent latitude bin. The equivalent latitude position of the dynamic tropopause (white circles) is shown on each isentrope as mean over all measurement days. Zonal mean zonal wind speed at all measurement days is represented by orange contours.

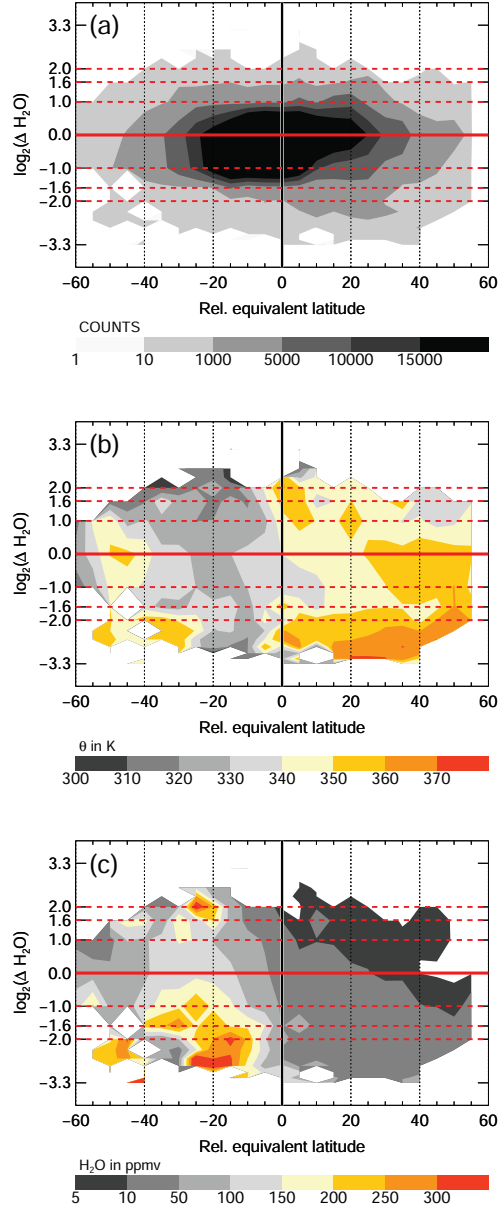


**Fig. 9.** Counts of data (panel a), mean potential temperature (panel b) and mean  $H_2O_{FISH}$  (panel c) of all Northern hemisphere measurement campaigns (TROCCINOX and SCOUT are excluded) plotted as averages per logarithmic  $\Delta H_2O_{ERA}^{\log 2}$  and  $5^\circ$  relative equivalent latitude difference bin with respect to the dynamic tropopause (see white circles in Fig. 8).

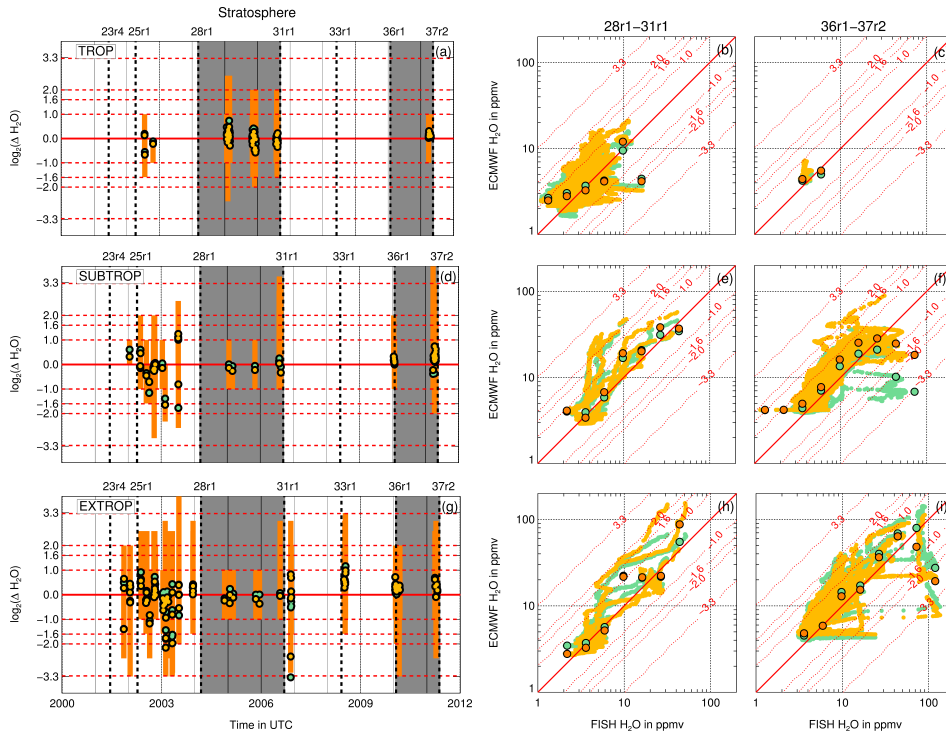


**Fig. 10.** Left panels: Daily mean  $\Delta H_2O^{\log 2}$  of operational analysis water vapor mixing ratio ( $H_2O_{ANA}$ , black-orange dots) over the time for stratospheric measurements in the tropical (panel a), subtropical (panel d), and extratropical domain (panel g). The range between the minimum and maximum value of  $\Delta H_2O_{ANA}^{\log 2}$  on each day is marked by the orange vertical bars, the daily mean  $\Delta H_2O_{ERA}^{\log 2}$  by the black-green dots. Dashed red lines indicate  $\Delta H_2O^{\log 2}$  between -3.32 and 3.32, black dashed lines indicate the dates when selected IFS cycles became operational. Right panels: Correlation of  $H_2O_{FISH}$  with  $H_2O_{ANA}$  (orange) and with  $H_2O_{ERA}$  (green) for two IFS cycle time periods (gray shadings, left panels). The first period, i.e., IFS cycles 28r1-31r1, include measurements from 09 March 2004 to 12 September 2006 (panels b, e, and h) and the second period, i.e., IFS cycles 36r1-37r2, measurements from 26 January 2010 to 18 May 2011 (panels c, f, and i). Means per  $H_2O_{FISH}$  bin are shown by black-surrounded larger dots.

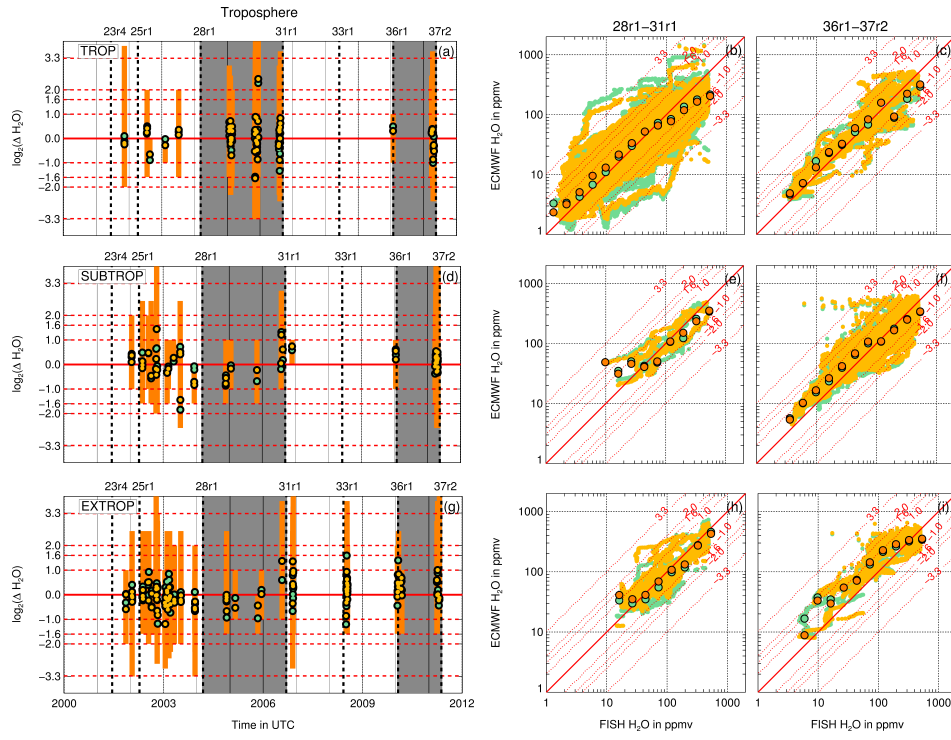


**Fig. 11.** As Figure 10 but for tropospheric measurements in the three different atmospheric domains.

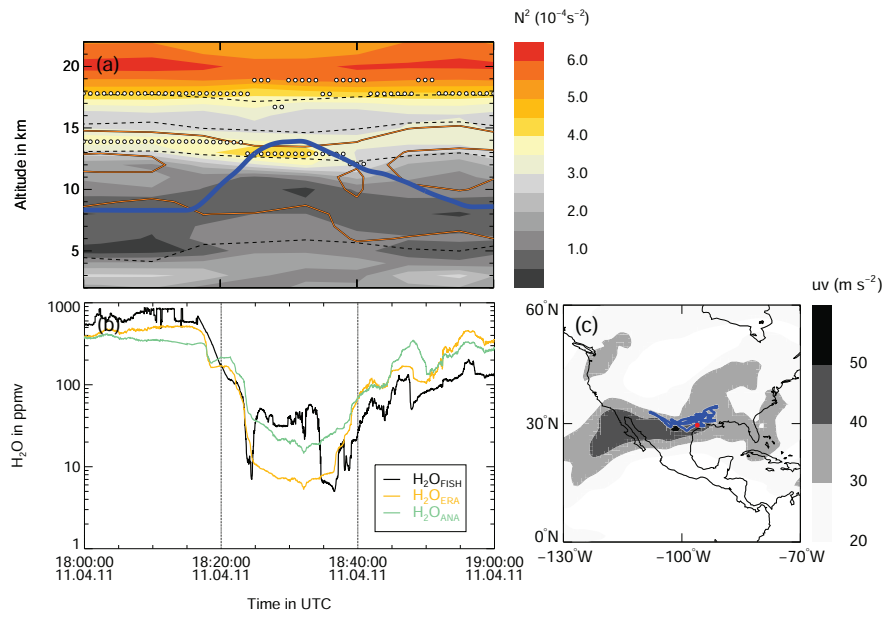


**Fig. 12.** Same as Fig. 3 but for a special flight segment during the MACPEX flight on 11 April 2011.